nature energy

SUPPLEMENTARY INFORMATION

https://doi.org/10.1038/s41560-020-0653-2

In the format provided by the authors and unedited.

A holistic approach to interface stabilization for efficient perovskite solar modules with over 2,000-hour operational stability

Zonghao Liu[1,2,5], Longbin Qiu[1,3,5], Luis K. Ono[1], Sisi He[1], Zhanhao Hu[1], Maowei Jiang[1], Guoqing Tong[1], Zhifang Wu[1], Yan Jiang[1], Dae-Yong Son[1], Yangyang Dang[1], Said Kazaoui[4] and Yabing Qi[1]✉

[1]Energy Materials and Surface Sciences Unit (EMSSU), Okinawa Institute of Science and Technology Graduate University (OIST), Okinawa, Japan. [2]Wuhan National Laboratory for Optoelectronics, Huazhong University of Science and Technology, Wuhan, China. [3]Department of Mechanical and Energy Engineering, Southern University of Science and Technology, Shenzhen, China. [4]Department of Energy and Environment, National Institute of Advanced Industrial Science and Technology (AIST), Tsukuba, Japan. [5]These authors contributed equally: Zonghao Liu, Longbin Qiu. ✉e-mail: Yabing.Qi@OIST.jp

Supplementary Information

A holistic approach to interface stabilization for efficient perovskite solar modules with over 2,000-hour operational stability

Zonghao Liu†[1,2], Longbin Qiu†[1,3], Luis K. Ono[1], Sisi He[1], Zhanhao Hu[1], Maowei Jiang[1], Guoqing Tong[1], Zhifang Wu[1], Yan Jiang[1], Dae-Yong Son[1], Yangyang Dang[1], Said Kazaoui[4], Yabing Qi*[1]

[1]Energy Materials and Surface Sciences Unit (EMSSU), Okinawa Institute of Science and Technology Graduate University (OIST), Okinawa, Japan

[2]Wuhan National Laboratory for Optoelectronics, Huazhong University of Science and Technology, Wuhan, China

[3]Department of Mechanical and Energy Engineering, Southern University of Science and Technology, Shenzhen, China

[4]Department of Energy and Environment, National Institute of Advanced Industrial Science and Technology (AIST), Tsukuba, Japan

† These authors contribute equally to this work.

*Corresponding author: Yabing Qi, E-Mail: Yabing.Qi@OIST.jp

Supplementary Figures:

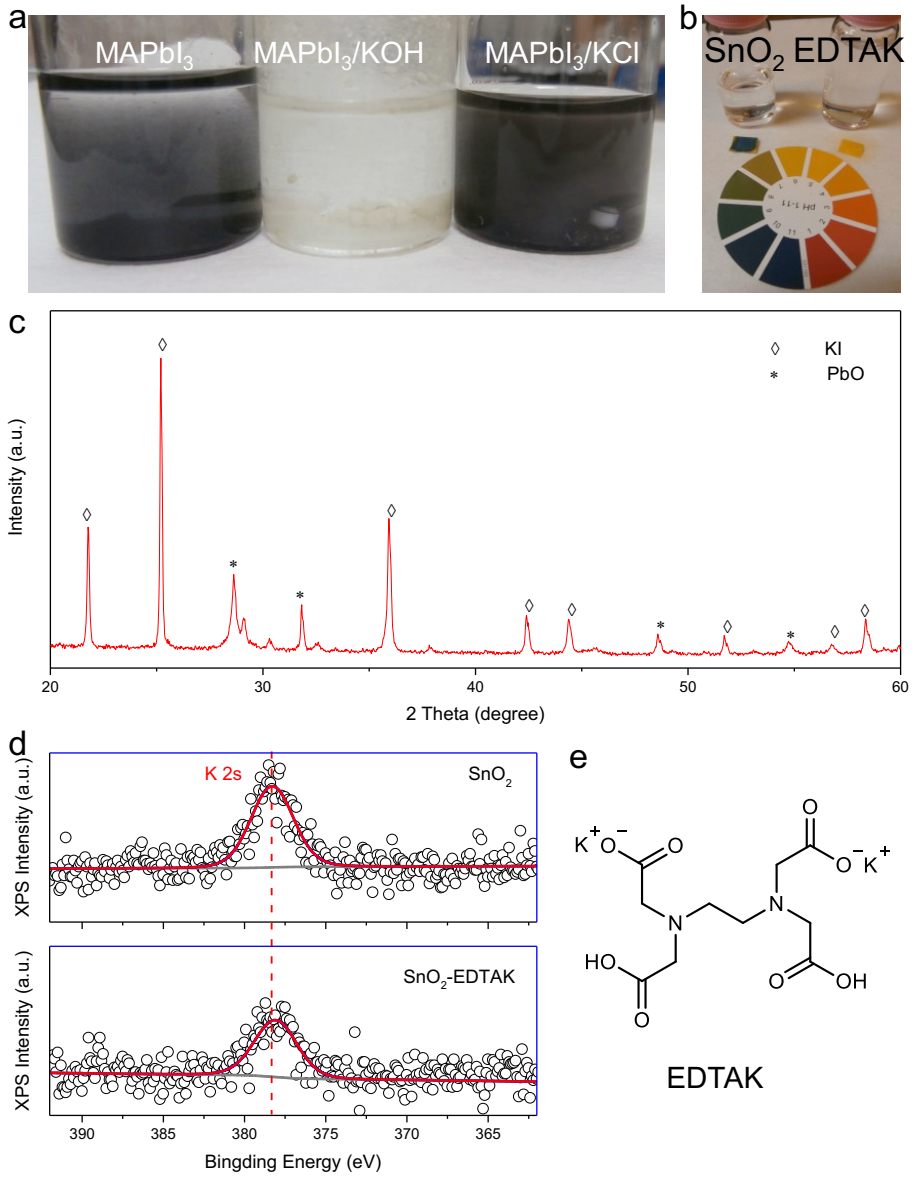

Supplementary Figure 1 | The chemical mitigation of KOH in commercial SnO_2 with EDTAK. (a) The optical image of $MAPbI_3$ powder (left), $MAPbI_3$/KOH powder (center) and $MAPbI_3$/KCl powder (right) in chlorobenzene mixed in a N_2 glove box after thorough stirring for 3 min. (b) The optical image shows the pH of the SnO_2 precursor solution and EDTAK solution. (c) The XRD spectrum of dried $MAPbI_3$/KOH powders measured under dry N_2 condition. (d) The XPS spectra showing the K 2*s* region of the SnO_2 and SnO_2-EDTAK films, background (grey), fitted result (red), K 2*s* position (vertical red dash line). (e) Molecular structure of EDTAK.

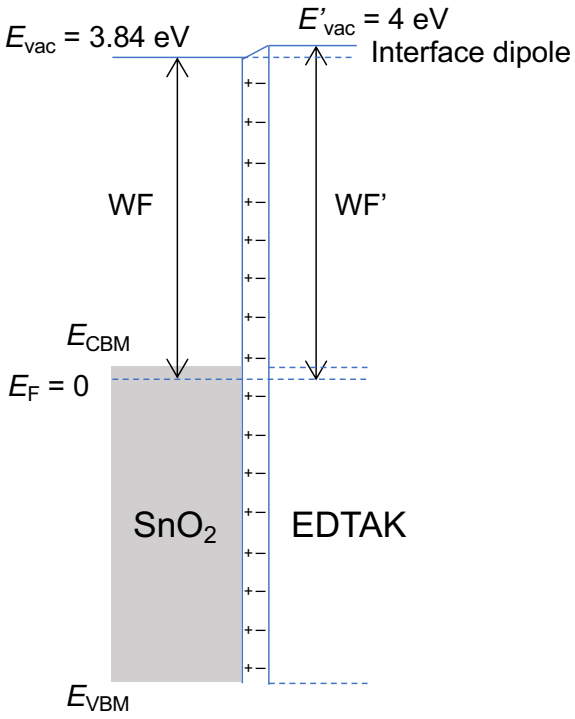

Supplementary Figure 2 | Schematic of energy level diagram of SnO_2 film with EDTAK modification.

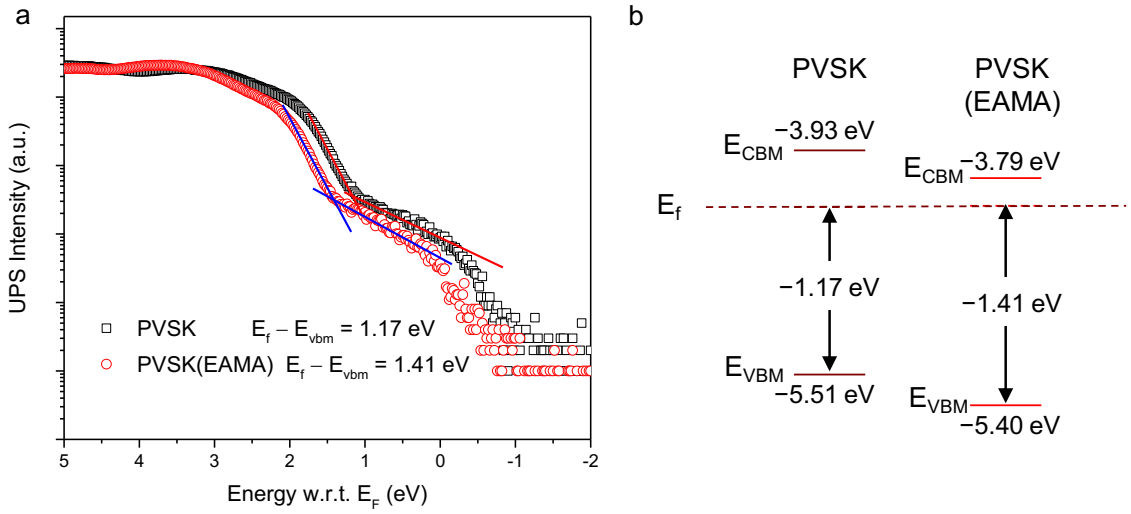

Supplementary Figure 3 | Schematic of energy-level diagram of perovskite film with EAI/MAI treatment. (a) The semi-logarithmic plot of the UPS spectra (using He-I with a photon energy of 21.22 eV) corresponding to the valence band region of the $Cs_{0.05}FA_{0.54}MA_{0.41}Pb(I_{0.98}Br_{0.02})_3$ (denoted as PVSK) and $Cs_{0.05}FA_{0.54}MA_{0.41}Pb(I_{0.98}Br_{0.02})_3$ with the EAI/MAI treatment (denoted as PVSK(EAMA)). (b) Energy diagram of PVSK and PVSK(EAMA), where E_F is the Fermi energy, E_{CBM} is the energy position of the conduction band minimum, and E_{VBM} is the energy position of the valance band maximum.

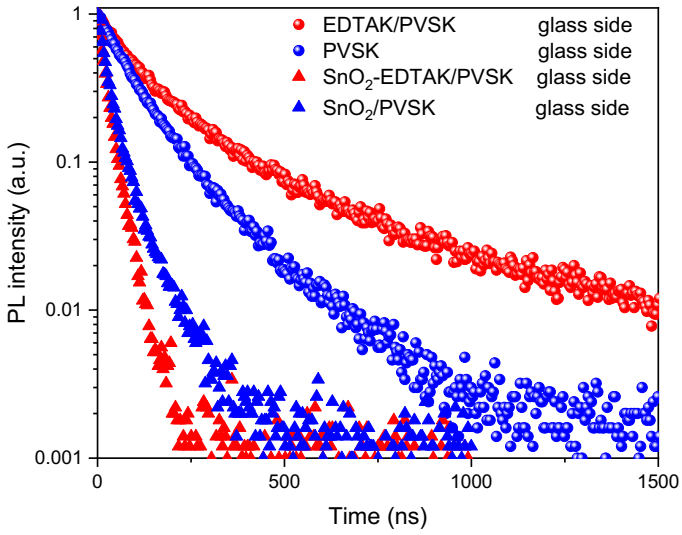

Supplementary Figure 4 | Time-resolved photoluminescence measurement of perovskite on different substrates. TRPL decay curves of the SnO_2/PVSK, SnO_2-EDTAK/PVSK, PVSK and EDTAK/PVSK samples, respectively. $Cs_{0.05}FA_{0.54}MA_{0.41}Pb(I_{0.98}Br_{0.02})_3$ perovskite is denoted as PVSK and $Cs_{0.05}FA_{0.54}MA_{0.41}Pb(I_{0.98}Br_{0.02})_3$ perovskite with the EAI/MAI treatment is denoted as PVSK(EAMA).

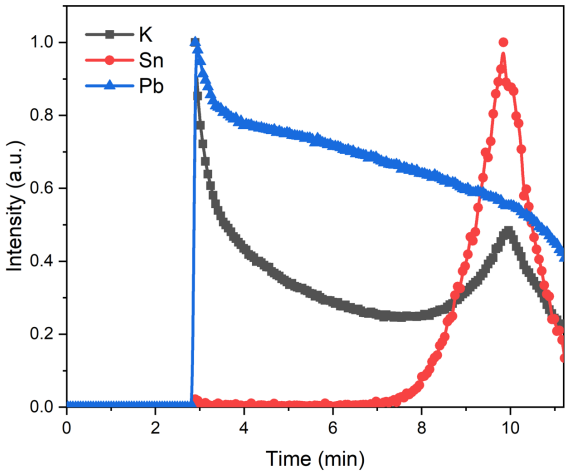

Supplementary Figure 5 | The distribution of potassium. The secondary ion mass spectrometry (SIMS) result of the ITO/SnO_2-EDTAK/PVSK sample to show the distribution of potassium.

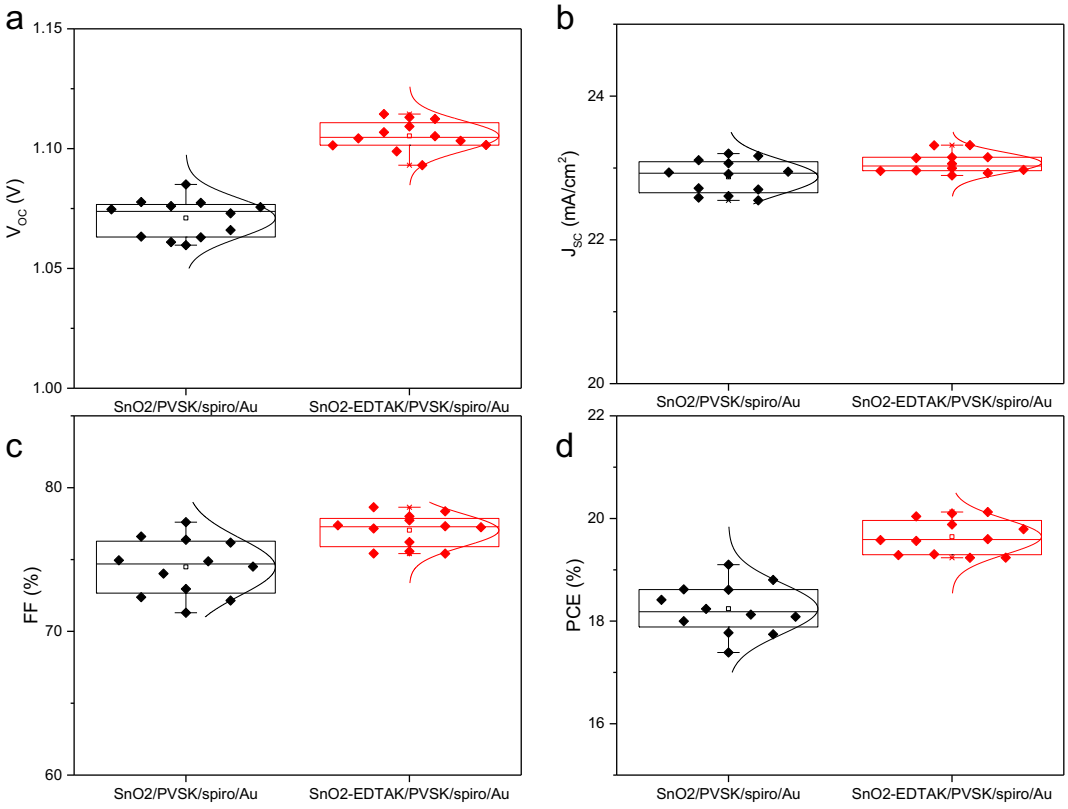

Supplementary Figure 6 | Photovoltaic performance of PSCs based on different electron transporting materials. The device performance statistics for 12 PSCs based on the SnO_2 and SnO_2-EDTAK film: (a) V_{OC}, (b) J_{SC}, (c) FF, (d) PCE. spiro stands for spiro-OMeTAD. In a typical box-and-whisker plot, the box represents the percentiles from 25% to 75%, the line in the box is the median line, the square in the center of the box is the mean point, the diamond solid black or red points are the data points, the black or red curve shows the lognormal distribution of the data points.

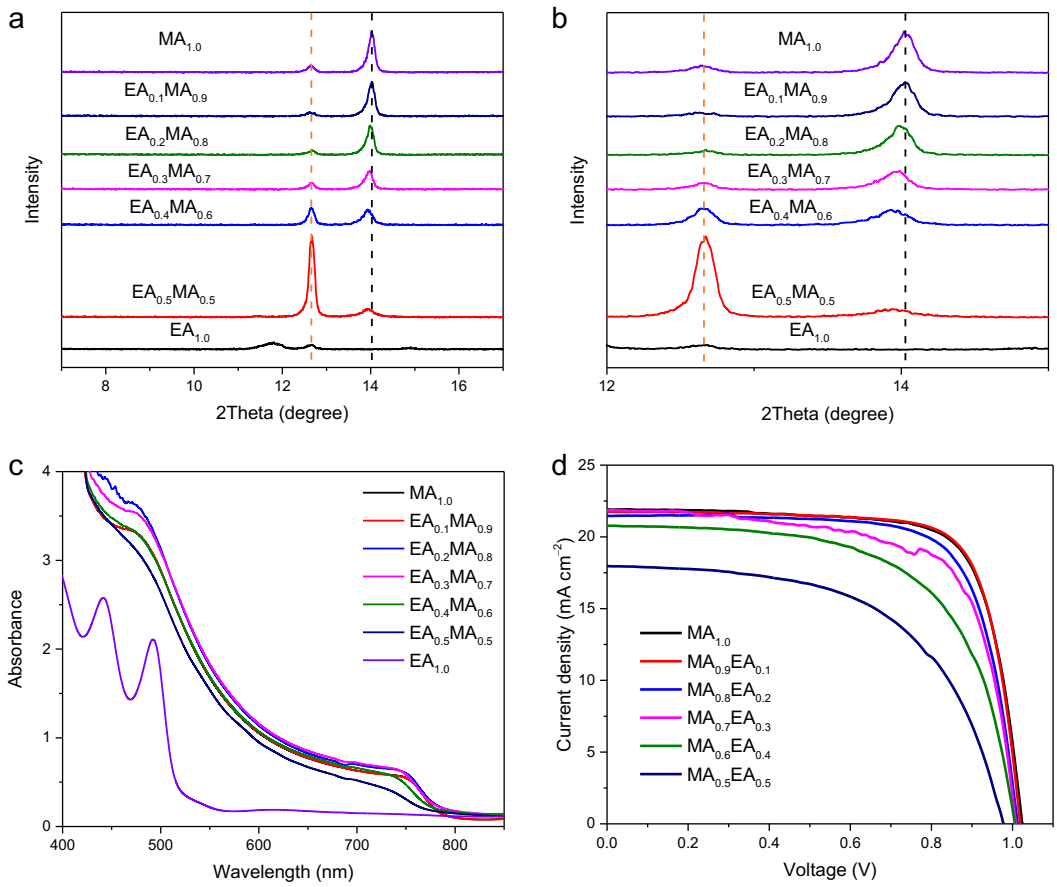

Supplementary Figure 7 | Optimization of EAI/MAI ratio. (a) and (b) The XRD spectra, (c) the UV-vis spectra of the $MA_{1-x}EA_xPbI_3$ films by reacting mixed EAI/MAI = x: (1−x) with PbI_2 films via the two-step method. (d) The current density-voltage curves of PSCs based on the $MA_{1-x}EA_xPbI_3$ films by reacting mixed EAI/MAI = x: (1−x) with PbI_2 films via the two-step method.

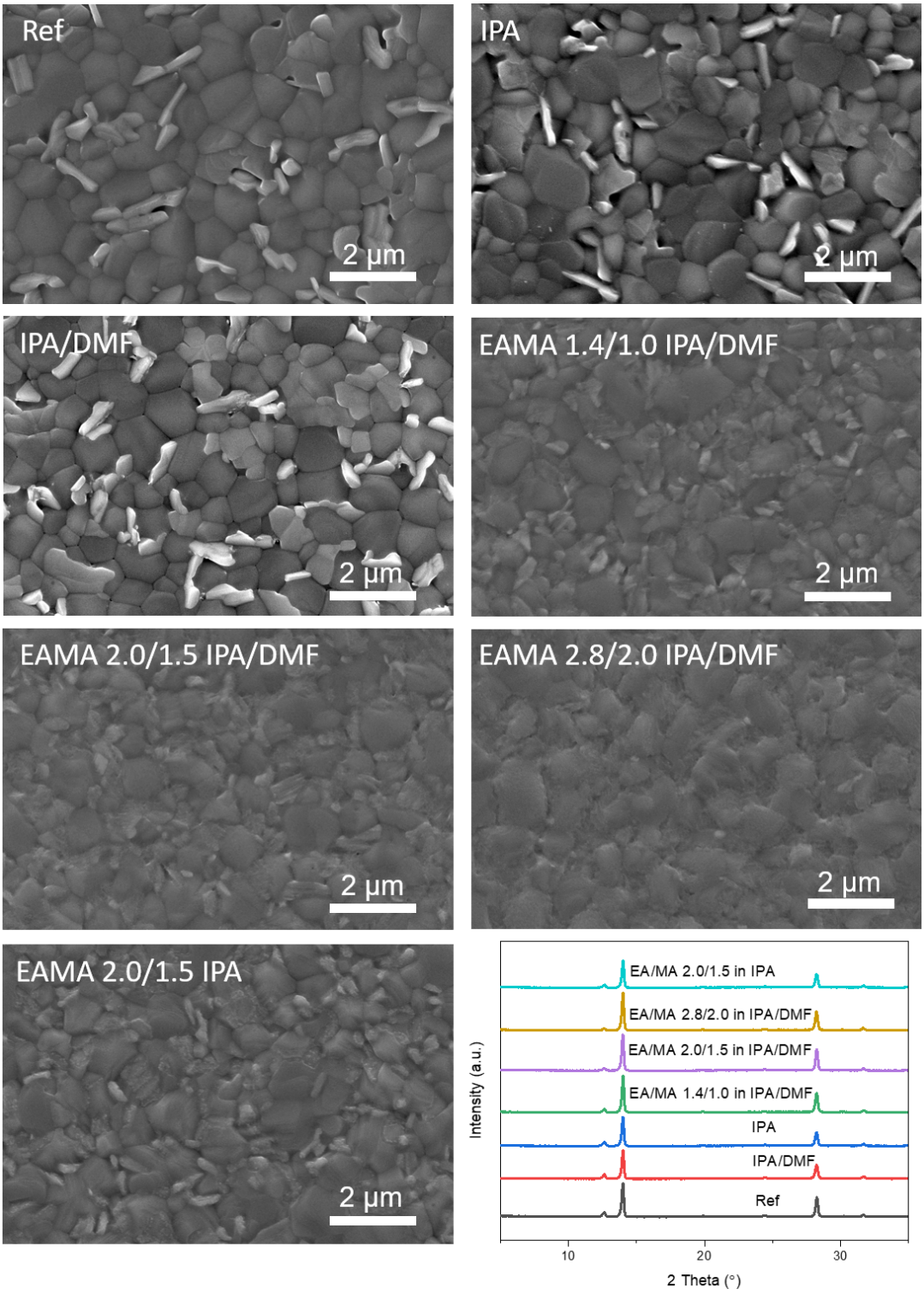

Supplementary Figure 8 | Morphology and crystallography study of perovskite films for optimization of EAI/MAI treatment condition. The SEM and XRD results for the perovskite sample with varying MAI/EAI concentrations in comparison with the control samples.

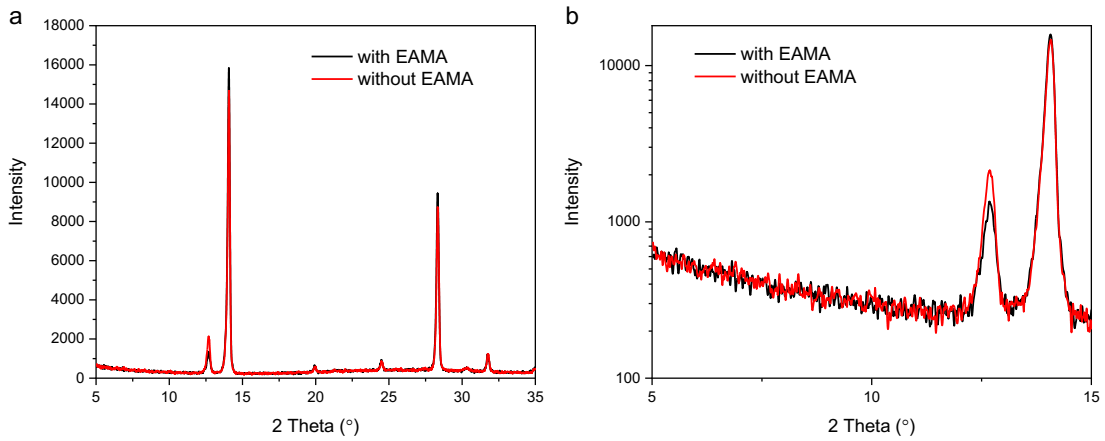

Supplementary Figure 9 | Crystallography study of perovskite films with and without EAI/MAI treatment. (a) The XRD spectra and (b) enlarged XRD (5-15°) spectra of the $Cs_{0.05}FA_{0.54}MA_{0.41}Pb(I_{0.98}Br_{0.02})_3$ films with and without the EAI/MAI treatment.

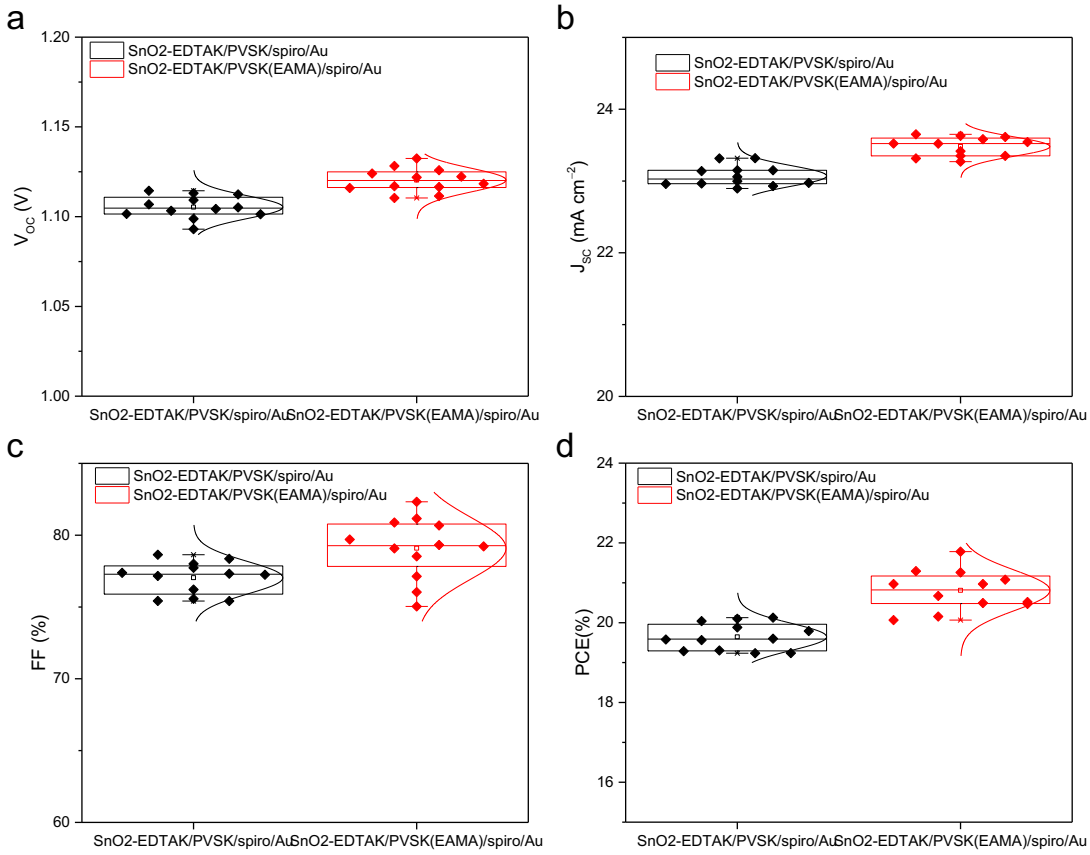

Supplementary Figure 10 | Photovoltaic performance of PSCs based on different perovskite films. The device performance statistics for 12 PSCs based on perovskite films with or without the EAI/MAI treatment: (a) V_{OC}, (b) J_{SC}, (c) FF, (d) PCE. spiro stands for spiro-OMeTAD. In a typical box-and-whisker plot, the box represents the percentiles from 25% to 75%, the line in the box is the median line, the square in the center of the box is the mean point, the diamond solid black or red points are the data points, the black or red curve shows the lognormal distribution of the data points.

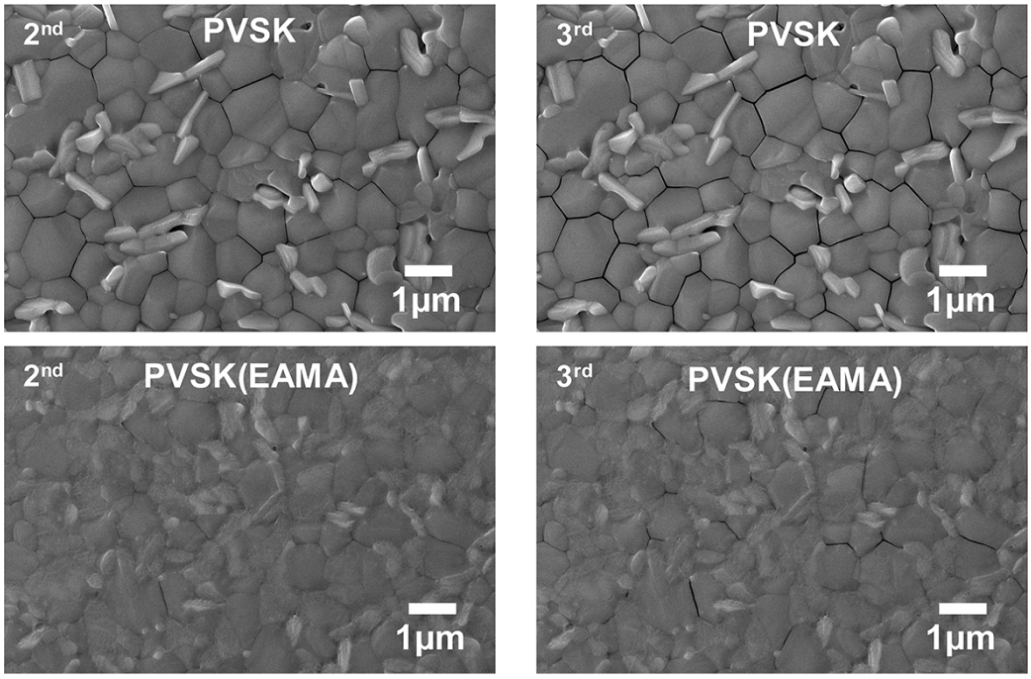

Supplementary Figure 11 | Morphology evolution of perovskite films under SEM beam. Surface SEM images of PVSK and PVSK(EAMA) films after high-energy electron beam scans with a voltage of 20 kV, (Figure 4 a-b show the first-scan SEM images, 2^{nd}, 3^{rd} represent images obtained from second and third SEM scan, respectively).

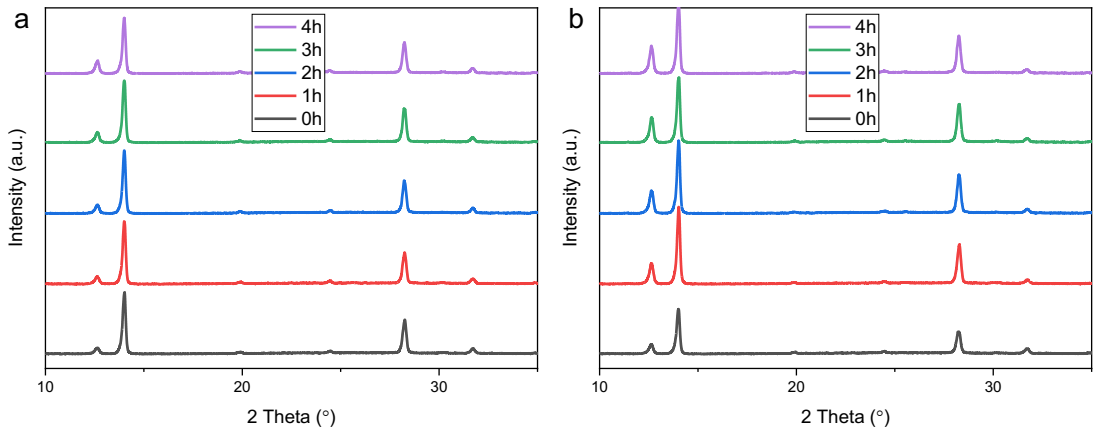

Supplementary Figure 12 | Thermal stability of perovskite films. Evolution of XRD patterns for the $Cs_{0.05}FA_{0.54}MA_{0.41}Pb(I_{0.98}Br_{0.02})_3$ film with (a) and without (b) the EAI/MAI treatment under thermal aging test on a hotplate at 85 ºC in a dry N_2 glove box.

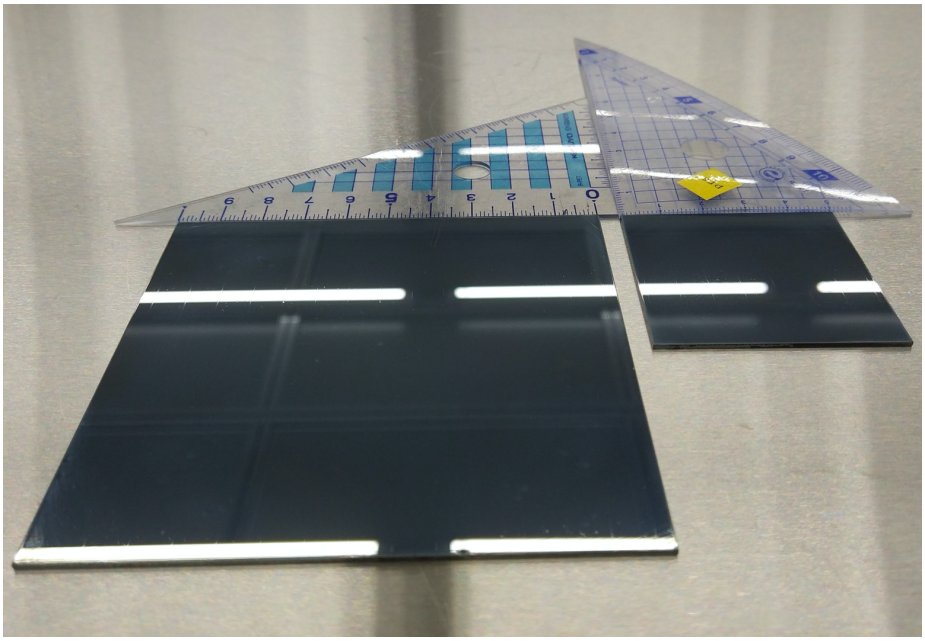

Supplementary Figure 13 | Optical image of large area perovskite films. The optical image of the large area (10 cm × 10 cm and 5 cm × 5 cm) $Cs_{0.05}FA_{0.54}MA_{0.41}Pb(I_{0.98}Br_{0.02})_3$ films via the two-step method.

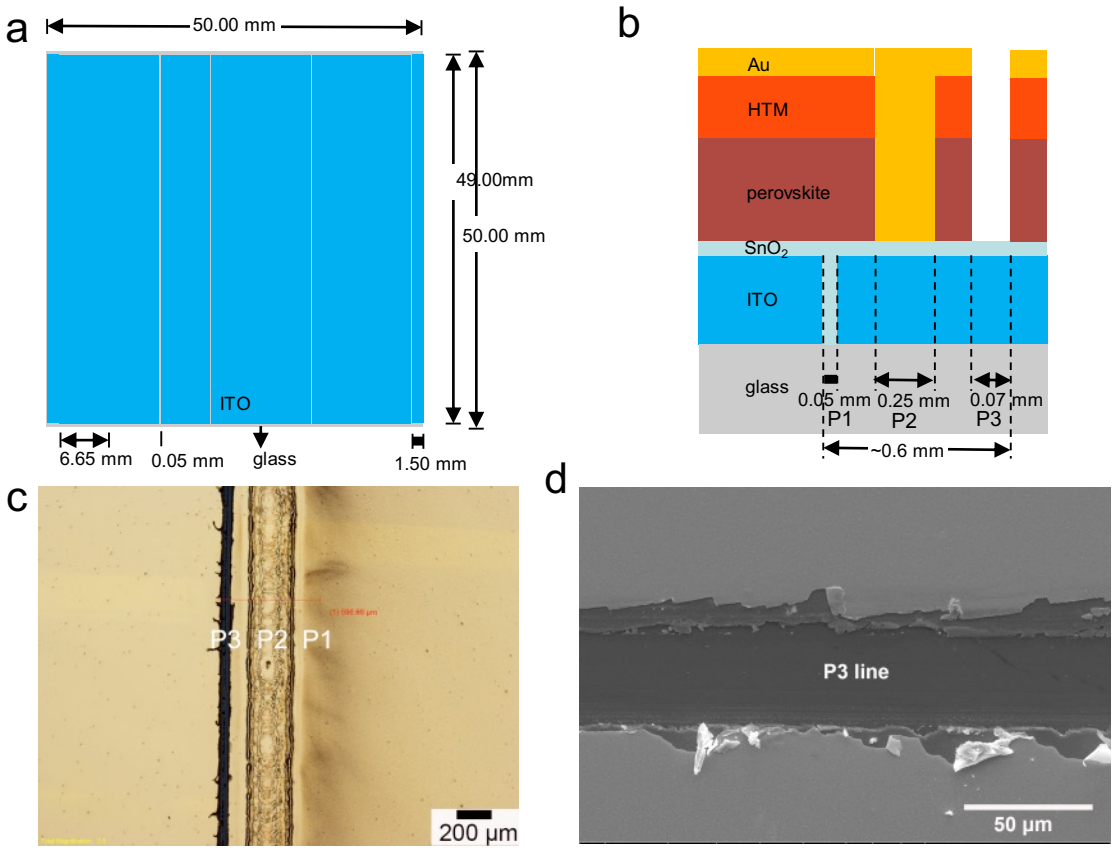

Supplementary Figure 14 | The geometry of the PSM. (a) Top view of the entire module, including the glass substrate, ITO pattern. (b) Side view of the module showing the solar module interconnections. (c) Optical photo of patterning for sub-cell separation in modules. The geometric fill factor (GFF) is determined to be approximately 0.91. (d) The SEM image of the P3 line of the PSM. It should be noted that there are some residues observed at the line edge of the P3 patterning. The residues are the active materials, including perovskite layer, HTL and gold layer, which were scraped off by the knife during scribing. Compared to other reports, the interconnection of our module needs to be further optimized.[1-3] Advanced interconnection preparation equipment such as a specially designed laser cutting system for preparing more accurate, clean interconnection lines is expected to further improve the device efficiency and stability.

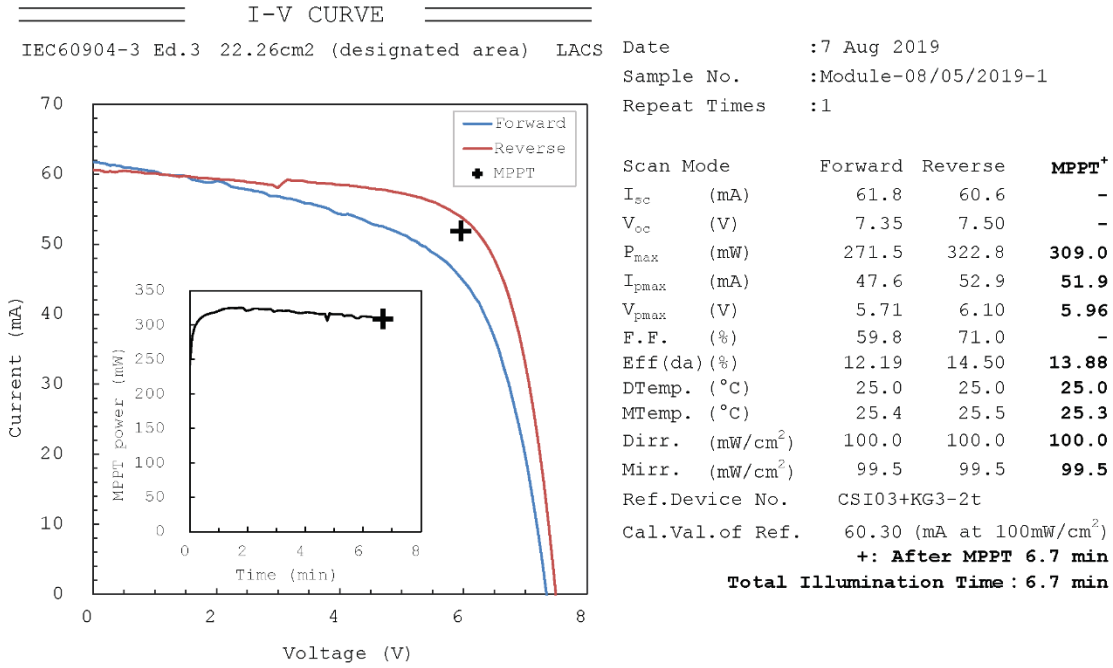

Supplementary Figure 15 | PSM performance measured by AIST. J-V curves of the encapsulated module covered by a black mask with a designated area of 22.26 cm^2 was measured by a public test centre (AIST), according to the well-established standard protocol (IEC60904-3 Ed. 3), which has recently also included maximum power point tracking (MPPT) suitable for perovskite solar cell devices that exhibit IV hysteresis. The J-V curves were recorded after tracking for 6.7 min at MPP under light illumination (marked with the symbol +). The PCE of 13.88% was obtained (marked with symbol +), which is between the reverse scan PCE of 14.50% and forward scan PCE of 12.19% as extracted from J-V scan. According to this protocol, the decrease in PCE is likely due to the burn-in process of the device under continuous MPPT and under continuous light illumination.[4] A fast decrease in PCE in the burn-in process is also observed during our stability tracking measurement performed in our laboratory (Figure 5). The initial maximum PCE is estimated to be approximately 15.4% under reverse J-V scan according to the results from AIST, which is consistent with the PCE of around 15.8% measured in our laboratory before we sent this solar module to AIST for testing (Supplementary Figure 16). Note that the Supplementary Figure 15 is not a certificate.

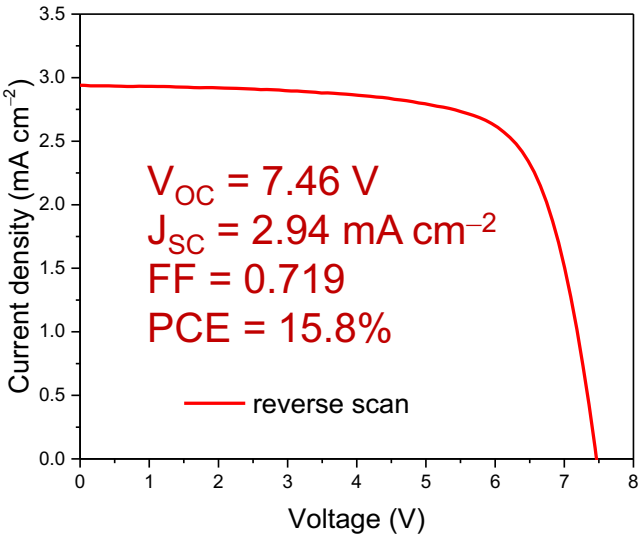

Supplementary Figure 16 | PSM performance measured by OIST. J-V curve of the encapsulated PSM measured in our laboratory before it was sent to AIST for characterization.

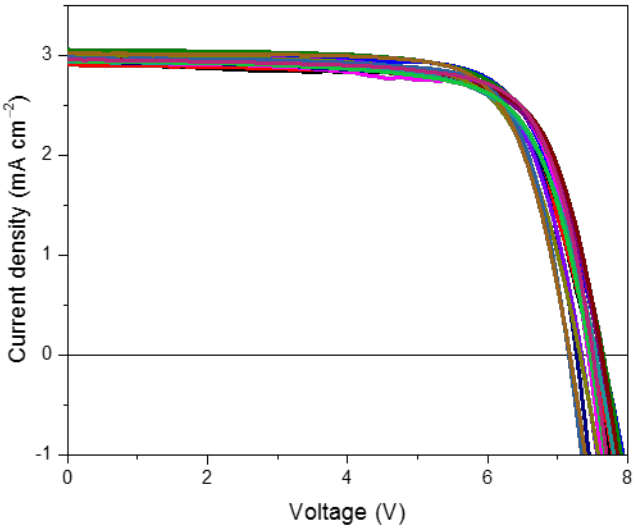

Supplementary Figure 17 | Statistic device performance of PSMs. The J-V curves of 15 samples of 5 cm × 5 cm SnO_2-EDTAK/PVSK(EAMA)/spiro-OMeTAD/Au solar modules.

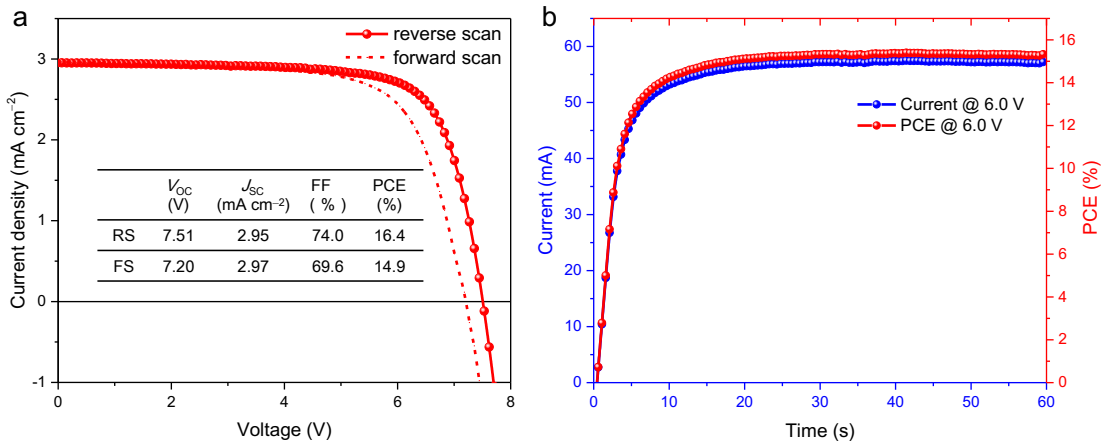

Supplementary Figure 18 | Hysteresis study of the PSM. (a) The J-V curves of reverse scan (RS) and forward scan (FS). (b) Stabilized output.

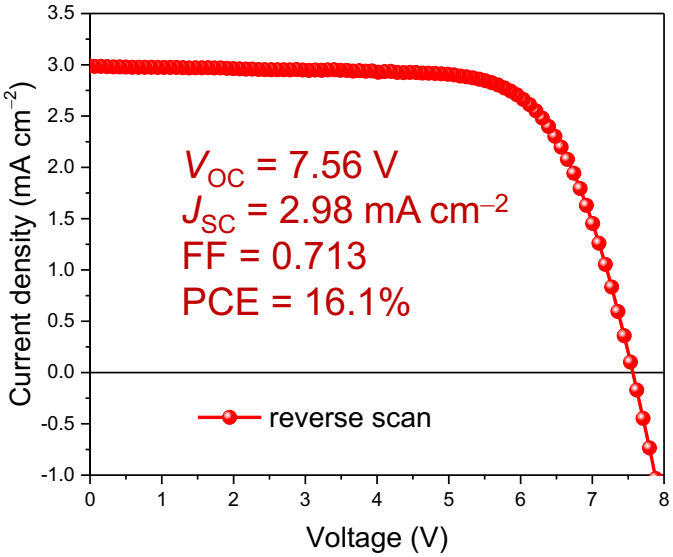

Supplementary Figure 19 | The typical J-V curve of a PSM based on mixed spiro-OMeTAD-P3HT HTL.

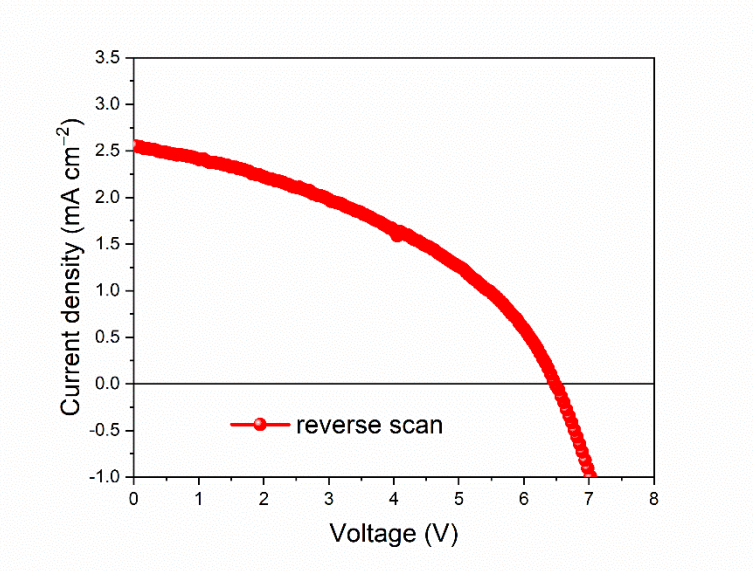

Supplementary Figure 20 | J-V curve of the PSM based on the P3HT-only HTL. PCE = 6.7%.

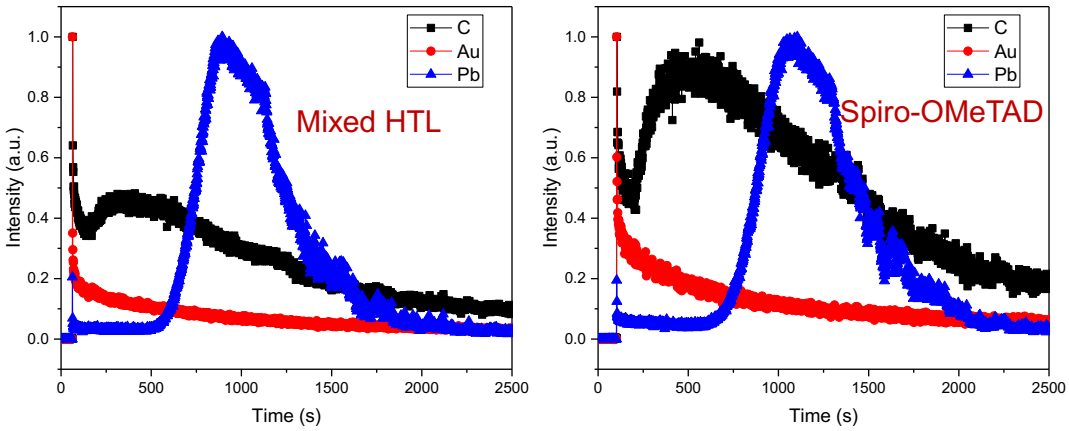

Supplementary Figure 21 | The element distribution of devices after thermal aging. The SIMS results of the aged device samples with mixed spiro-OMeTAD-P3HT (mixed HTL) and spiro-OMeTAD.

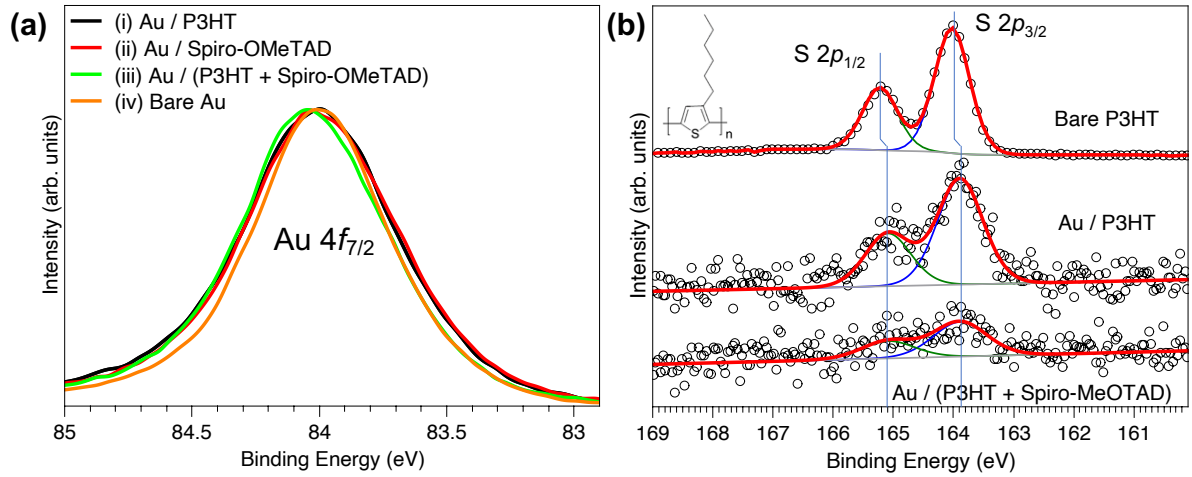

Supplementary Figure 22 | The interaction of HTLs with Au. XPS spectra (Al−Kα = 1486.6 eV; 150 W) corresponding to (a) the Au 4$f_{7/2}$ and (b) S 2p core levels of Au (thickness ~ 2 nm) deposited on (i) P3HT, (ii) spiro-OMeTAD, (iii) P3HT + spiro-OMeTAD mixed HTL, and the bare Au (20 nm) and P3HT as the reference samples. ITO/glass substrates were used for all samples.

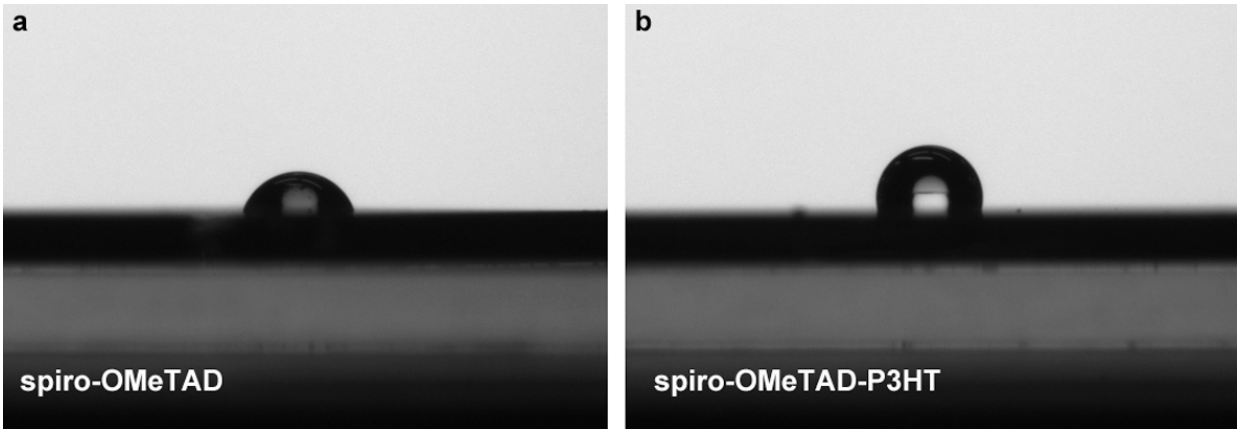

Supplementary Figure 23 | The contact angles HTLs. Photographs of the contact angle measurements for the (a) ITO/Sn_2O-EDTAK/perovskite/spiro-OMeTAD sample (denoted as spiro-OMeTAD in the image) and (b) ITO/Sn_2O-EDTAK/perovskite/spiro-OMeTAD-P3HT sample (denoted as spiro-OMeTAD-P3HT in the image). The contact angle is measured to be 71.6^o and 107.0^o, respectively.

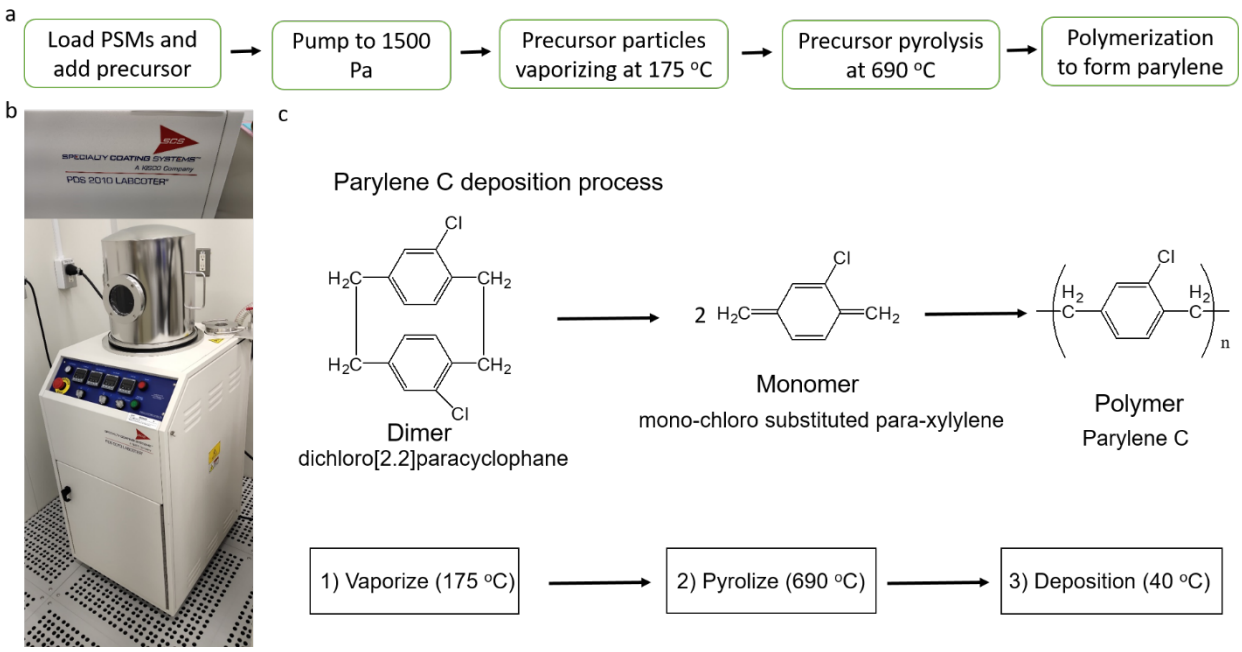

Supplementary Figure 24 | Parylene encapsulation. (a) The flow diagram, (b) parylene deposition equipment (PDS 2010 LABCOATER) and (c) reaction mechanism for parylene deposition.

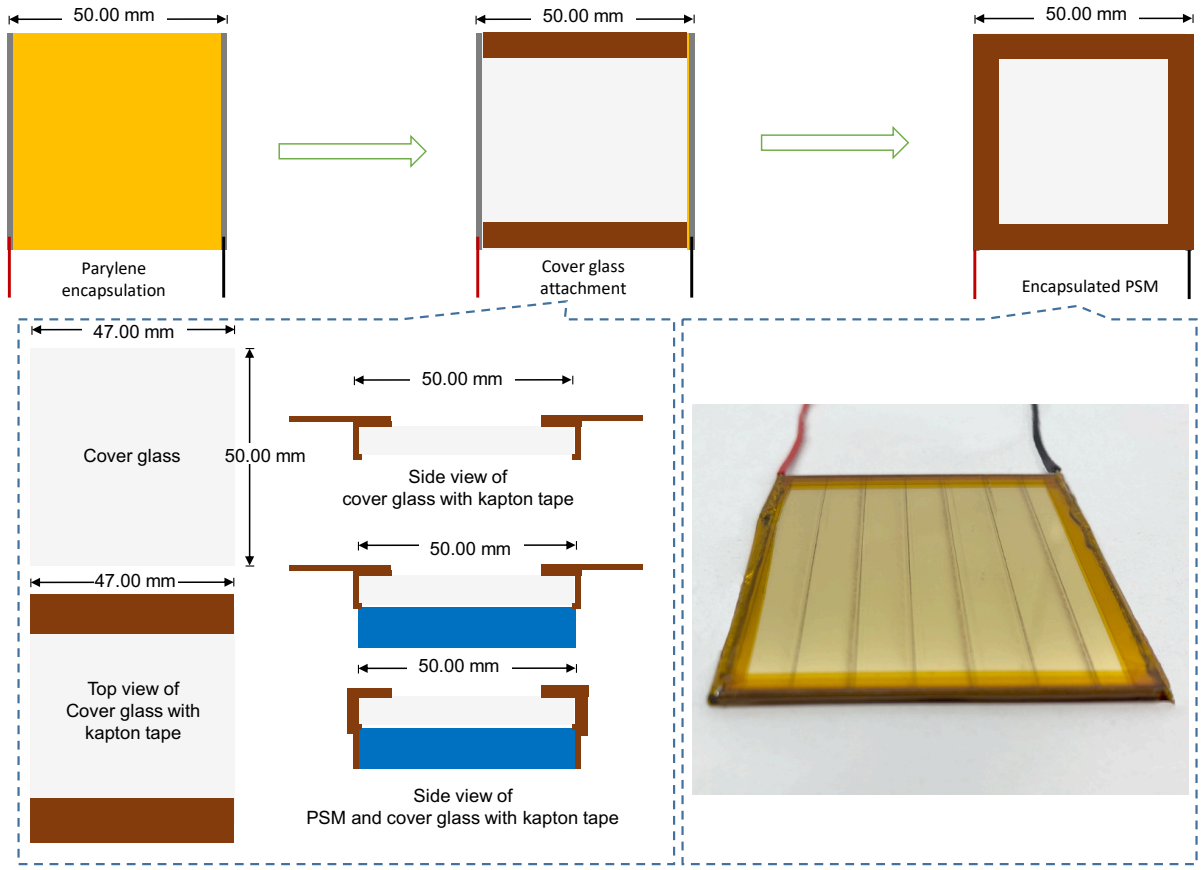

Supplementary Figure 25 | PSM encapsulation. The flow diagram for the PSM encapsulation with parylene and cover glass encapsulation.

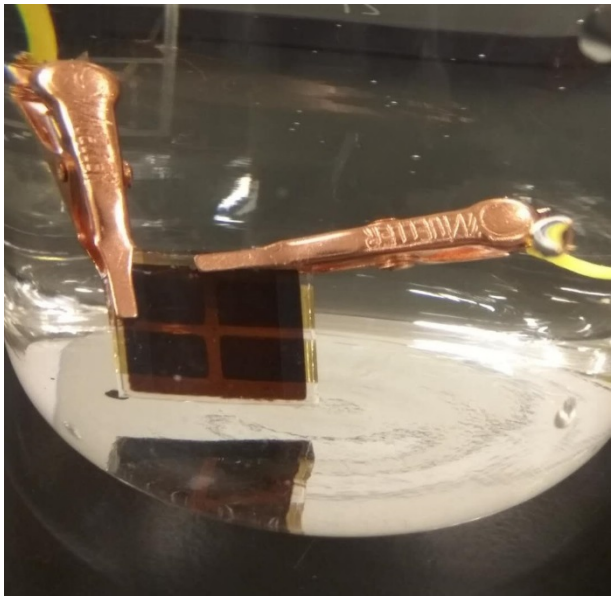

Supplementary Figure 26 | Waterproof properties of device with parylene encapsulation. Photograph of a perovskite solar cell encapsulated with parylene that was immersed into water. No obvious color change was overserved for this device after being kept in water for 10 min, which means the parylene can act as a robust barrier to protect the under layers against the ingress of H_2O.

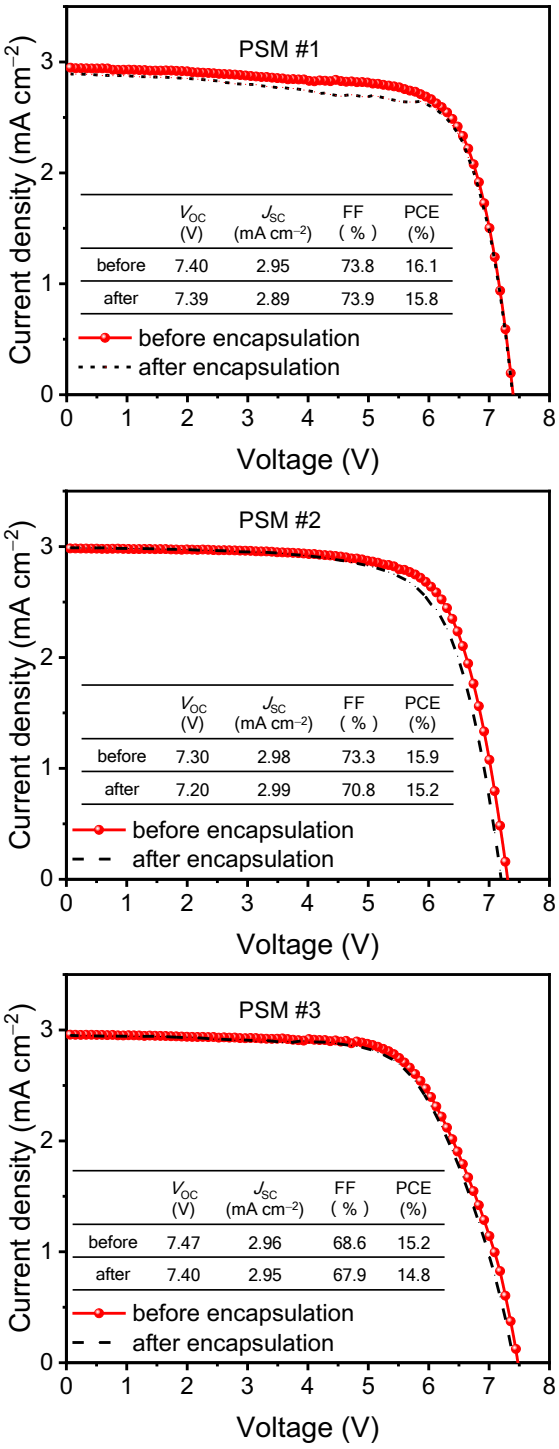

Supplementary Figure 27 | PSMs performance before and after encapsulation. J-V curves of the SnO_2-EDTAK/PVSK(EAMA)/spiro-OMeTAD-P3HT/Au PSM before and after being encapsulated with parylene and a cover glass for operational stability test. Upper, middle and bottom panel show the J-V curves for PSM #1, #2 and #3, respectively.

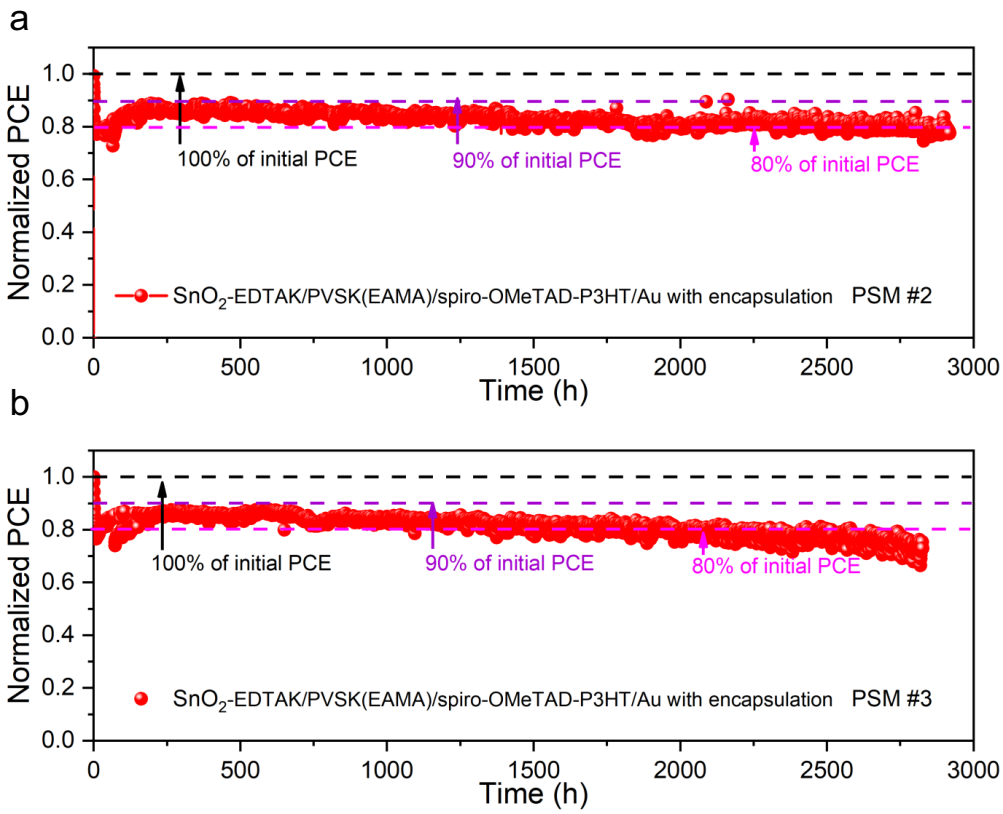

Supplementary Figure 28 | Operational stability of encapsulated PSMs. Operational stability measurement results of the two additional encapsulated SnO_2-EDTAK/PVSK(EAMA)/spiro-OMeTAD-P3HT/Au solar modules (PSM #2, initial PCE= 15.2%, T_{80} = 2540 h; PSM #3, initial PCE = 14.8%, T_{80} = 2150 h; the sample in Figure 5d is PSM #1) with parylene encapsulation and a cover glass examined under continuous full-sun illumination in dry N_2 atmosphere.

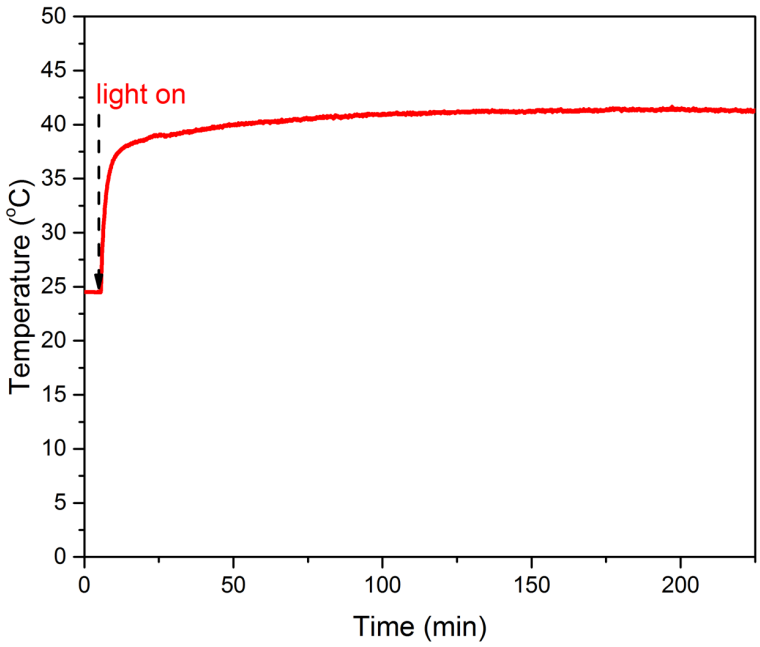

Supplementary Figure 29 | The temperature of the top surface of the PSM during stability tracking. The temperature was measured to be approximately 40 °C.

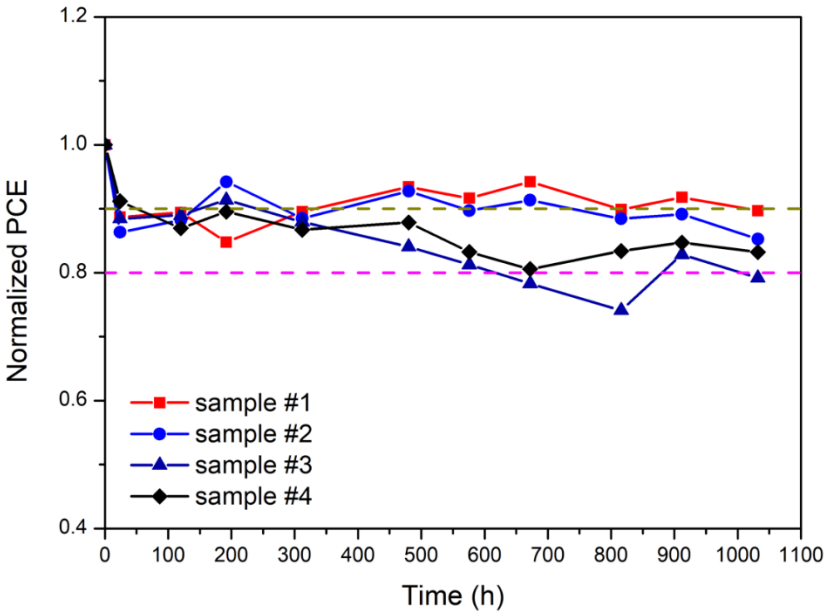

Supplementary Figure 30 | Thermal stability of PSMs. The PCEs evolution of the four encapsulated PSMs under thermal heating at 60 °C in a N_2 glove box with relative humidity lower than 5%. The detailed PV values are listed in Supplementary Table 8.

Supplementary Tables:

Supplementary Table 1 | Summarized J-V characteristics of the best devices with the varying EDTAK concentration in comparison with the control device:

sample	V_{OC} (V)	J_{SC} (mA cm^{-2})	FF (%)	PCE (%)
control	1.066	23.2	77.6	19.2
1.0 mM	1.085	23.2	77.7	19.6
2.5 mM	1.102	23.3	78.4	20.1
5.0 mM	1.091	23.1	75.3	19.0

Supplementary Table 2 | PL lifetimes extracted from the TRPL spectra of the SnO_2/PVSK, SnO_2-EDTAK/PVSK, glass/PVSK and glass/EDTAK/PVSK samples, respectively. PVSK is $Cs_{0.05}FA_{0.54}MA_{0.41}Pb(I_{0.98}Br_{0.02})_3$ perovskite. A bi-exponential function is used to fit the curves.

	τ_1 (ns)	A_1	τ_2 (ns)	A_2	$\tau_{average}$ (ns)
EDTAK/PVSK	78.7	0.596	280.0	0.404	160.0
PVSK	75.8	0.717	185.0	0.272	104.7
SnO_2-EDTAK/PVSK	20.0	0.877	48.5	0.137	24.2
SnO_2/PVSK	24.2	0.767	67.0	0.243	34.8

Supplementary Table 3 | Summary of the device performance of the PSCs with ETL and HTL interface treatments, respectively. H-index is defined as follows as a measure of the hysteresis in the J-V curve: H-index = $(PCE_{reverse}-PCE_{Forward})/PCE_{Reverse}$. $PCE_{reverse}$ and $PCE_{forward}$ are PCEs from the reverse and forward scan, respectively.

Device	Scan	V_{OC} (V)	J_{SC} (mA cm^{-2})	FF (%)	PCE (%)	H-index
SnO_2/PVSK/spiro-OMeTAD/Au	RS	1.07	23.2	77.6	19.2	0.104
	FS	1.07	23.3	68.9	17.2	
SnO_2-EDTAK/PVSK/spiro-OMeTAD/Au	RS	1.10	23.2	78.4	20.1	0.079
	FS	1.10	23.2	72.6	18.5	
SnO_2-EDTAK/PVSK(EAMA)/spiro-OMeTAD/Au	RS	1.12	23.6	82.3	21.8	0.041
	FS	1.12	23.5	79.3	20.9	

Supplementary Table 4 | Summarized J-V characteristics of the best devices with the varying MAI/EAI concentration (IPA/DMF as solvent) in comparison with the control device:

solvent	MAI/EAI (mg/mL)	V_{OC} (V)	J_{SC} (mA cm^{-2})	FF (%)	PCE (%)
Ref.	Ref.	1.102	23.3	78.4	20.1
IPA	0.0/0.0	1.065	22.7	74.2	17.9
IPA/DMF	0.0/0.0	1.069	23.0	74.9	18.4
IPA/DMF	1.4/1.0	1.110	23.4	80.5	20.9
IPA/DMF	2.0/1.5	1.122	23.6	82.3	21.8
IPA/DMF	2.8/2.0	1.103	23.0	80.6	20.4
IPA	2.0/1.5	1.089	22.9	79.4	19.8

Supplementary Table 5 | PL lifetimes and diffusion lengths extracted from the TRPL spectra of glass/PVSK, glass/PVSK(EAMA), glass/PVSK/spiro-OMeTAD and glass/PVSK(EAMA)/spiro-OMeTAD samples, respectively. PVSK is $Cs_{0.05}FA_{0.54}MA_{0.41}Pb(I_{0.98}Br_{0.02})_3$ perovskite. A bi-exponential function is used to fit the curves.

	τ_1 (ns)	A_1	τ_2 (ns)	A_2	$\tau_{average}$ (ns)
PVSK	19.1	0.859	84.9	0.311	42.8
PVSK(EAMA)	52.2	0.644	242.5	0.366	122.4
PVSK/spiro-OMeTAD	13.7	0.626	13.7	0.413	13.7
PVSK(EAMA)/spiro-OMeTAD	10.0	0.795	10.0	0.228	10.0

Supplementary Table 6 | The device performance parameters of SnO_2/PVSK/spiro-OMeTAD/Au module, SnO_2-EDTAK/PVSK/spiro-OMeTAD/Au module, and SnO_2-EDTAK/PVSK(EAMA)/spiro-OMeTAD/Au module, SnO_2-EDTAK/PVSK(EAMA)/spiro-OMeTAD-P3HT/Au module.

module	V_{OC} (V)	J_{SC} (mA cm^{-2})	FF (%)	PCE (%)
SnO_2/PVSK/spiro-OMeTAD/Au	6.89	2.96	55.7	11.4
SnO_2-EDTAK/PVSK/spiro-OMeTAD/Au	7.15	2.96	64.9	13.7
SnO_2-EDTAK/PVSK(EAMA)/spiro-OMeTAD/Au	7.64	2.99	72.9	16.6
SnO_2-EDTAK/PVSK(EAMA)/spiro-OMeTAD-P3HT/Au	7.56	2.98	71.3	16.1

Supplementary Table 7 | The device performance parameters of 15 samples of 5 cm × 5 cm SnO_2-EDTAK/PVSK(EAMA)/spiro-OMeTAD/Au module devices.

sample	V_{OC} (V)	J_{SC} (mA cm^{-2})	FF (%)	PCE (%)
1	7.50	2.90	71.9	15.7
2	7.55	2.93	70.6	15.6
3	7.47	2.92	72.3	15.8
4	7.61	2.98	70.4	16.0
5	7.63	3.00	70.8	16.2
6	7.32	3.00	71.2	15.6
7	7.64	2.99	72.9	16.6
8	7.34	2.99	72.9	16.0
9	7.17	3.02	74.5	16.2
10	7.16	2.97	75.7	16.1
11	7.50	2.95	74.0	16.4
12	7.49	2.94	71.3	15.7
13	7.27	2.93	74.4	15.9
14	7.44	2.94	73.6	16.1
15	7.65	3.05	70.8	16.5
Average	7.44±0.16	2.97±0.04	72.5±1.6	16.0±0.3

Supplementary Table 8 | Thermal stability of PSMs. The PCEs evolution of the encapsulated PSMSs under thermal heating at 60 ºC in a N_2 glove box with relative humidity lower than 5%.

Time (h)	PCE (%) Sample #1	PCE (%) Sample #2	PCE (%) Sample #3	PCE (%) Sample #4
0	15.6	15.3	14.9	15.5
24	13.8	13.2	13.2	14.1
120	14.0	13.5	13.3	13.5
192	13.2	14.4	13.6	13.9
312	13.9	13.5	13.1	13.4
480	14.6	14.2	12.5	13.6
576	14.3	13.7	12.1	12.9
672	14.7	13.9	11.7	12.5
816	14.0	13.5	11.0	12.9
912	14.3	13.6	12.3	13.1
1032	14.0	13.0	11.8	12.9

Supplementary Table 9 | Characteristics of the perovskite solar modules with an active area ≥ 20 cm^2 and PCE ≥ 10% reported in the literature and in this work. The provided PCE values are normalized by the active area unless otherwise stated: ap, aperture area; da, designated area (active area + dead area for interconnections). SS: storage stability; LS: light soaking stability; WS: working stability; CE: certified efficiency. ITO, indium tin oxide; FTO, fluorine doped tin oxide; c-TiO_2, compact TiO_2; mp-TiO_2, mesoporous TiO_2; spiro-MeOTAD, 2,2′,7,7′-tetrakis(*N*,*N*-di-4-methoxyphenylamino)-9,9′-spirobifluorene; PCBM, [6,6]-phenyl-C60,61 butyric acid methyl ester; PTAA, poly[bis(4-phenyl)(2,4,6-trimethylphenyl)amine]; PEDOT:PSS, poly(3,4-ethylenedioxythiophene):poly(styrenesulfonate); P3HT, poly(3-hexylthiophene-2,5-diyl) regioregular; PC71BM, [6,6]-phenyl C71 butyric acid methyl ester; BCP, bathocuproine; 5-AVA, 5-aminovaleric acid.

Device structure	Module size (cm×cm)	Device area (cm^2)	Active area module PCE[a] (%)	Module stability (h)	Ref
ITO/PEDOT:PSS/$MAPbI_3$/PCBM/LiF/Al	10×10	60	8.7	–	5
ITO/PEDOT:PSS/$MAPbI_3$/PCBM/Au	10×10	40	12.9	–	6
ITO/PEDOT:PSS/$CH_3NH_3PbI_{3-x-y}Br_xCl_y$/PCBM/Ca/Al	10×10	25.2	14.3	–	7
FTO/c-TiO_2/mp-TiO_2/Graphene/$MAPbI_3$/Spiro-MeOTAD/Au	10×10	50.6	12.6	$>1630^{SS,T80}$	8
FTO/SnO_2/$K_xCs_{0.05}(FA_{0.85}MA_{0.15})_{0.92}Pb(I_{0.85}Br_{0.15})_3$/spiro-MeOTAD/Au	6×6	20	15.6	–	9
FTO/SnO_2/$MAPbI_3$/spiro-MeOTAD/Au	5×5	22.4^{da}	12.03	$515^{WS, T80}$	10
FTO/c-TiO_2/mp-TiO_2 /$(FAPbI_3)_{0.95}(MAPbBr_3)_{0.05}$/WBH/P3HT/Au	7×7	24.94^{da}	17.1	–	11
ITO/PTAA/$MAPbI_3$/C60/BCP/Cu	6×15	33	15.3	$480^{SS, about T100}$	12
		57.2	14.6		
PET/ITO/ZnO/$MAPbI_3$/P3HT/Ag	12.5×13.5	151.9	11.1	–	13
	11.5×11	142	11.8		
ITO/Cu-oxide/$MAPbI_{2.7}Br_{0.3}$/PCBM/BCP/Ag		25	15	–	14
FTO/c-TiO_2/(m-TiO_2/m-ZrO_2/m-C)/$(5\text{-AVA})_x(MA)_{1-x}PbI_3$	5×10	31	10.5	$2000^{SS,T95}$ $72^{WS,T96}$	15
	10×10	70	10.7		
FTO/c-TiO_2/(m-TiO_2/m-ZrO_2/m-C)/$(5\text{-AVA})_x(MA)_{1-x}PbI_3$	10×10	49	10.4	Light soaking stable	16
FTO/c-TiO_2/(m-TiO_2/m-ZrO_2/m-C)/$(5\text{-AVA})_x(MA)_{1-x}PbI_3$	10×10	46.7	11.2	$>10{,}000\ h^{WS}$	17
FTO/c-TiO_2/$MAPbI_{3-x}Cl_x$/PTAA/Au	10×10	40	15.5	–	18
FTO/c-TiO_2/mp-TiO_2/$MAPbI_3$/spiro-MeOTAD/Au	8×8	36.1^{ap}	15.7 (12.1^{CE})	$500^{WS,T90, 0.1 Sun}$	19
FTO/SnO_2/$(FA_{0.85}MA_{0.15})_{0.95}Pb(I_{0.85}Br_{0.15})_3$/spiro-MeOTAD/Au	10×10	53.6	13.9	–	20
FTO/SnO_2/C_{60}/$Cs_{0.1}FA_{0.9}PbI_3$/spiro-MeOTAD/Au	10×10	82.6	10.37	$500^{WS, T80,}$	21
FTO/SnO_2/$Cs_xFA_{1-x}PbI_{3-y}Br_y$/spiro-MeOTAD/Au	8×8	41.25	12.24	$200^{SS,T83}$	22
FTO/SnO_2/$K_xCs_{0.05}(FA_{0.85}MA_{0.15})_{0.92}Pb(I_{0.85}Br_{0.15})_3$/spiro-MeOTAD/Au	7×7	20.78	16.5^{CE}	–	23
ITO/C60/$MAPbI_3$/spiro-MeOTAD/Au	10×10	37.1	13.98^{CE}	$384^{SS,T60}$	24
ITO/C60/$MAPbI_3$/spiro-MeOTAD/Cu	10×10	37.1	11.09	$720^{SS,T90}$	
FTO/NiO/$FA_{0.85}MA_{0.15}Pb(I_{0.85}Br_{0.15})_3$/G-PCBM/BCP/Ag	6×6	35.8^{da}	15.6^{da} (14.17^{CE})	$1000^{LS, T91, with UV filter}$	25

ITO/SnO_2-EDTAK/$Cs_{0.05}FA_{0.54}MA_{0.41}Pb(I_{0.98}Br_{0.02})_3$ (EAMA)/spiro-MeOTAD-P3HT/Au with encapsulation	5×5	22.4 [da]	18.2	1570 [WS,T90] 2680 [WS,T80]	This work

Supplementary Notes:

Supplementary Note 1

It has been reported that K^+ is present in the form of KOH in commercial SnO_2 solution, which is added to stabilize the SnO_2 colloids.[26] Although strong alkaline KOH has been reported to induce formation of the δ-phase perovskite for the FAMA based perovskite, the reaction of OH^- with perovskite has not been fully studied.[27] Here, we investigated its effect by mixing the $CH_3NH_3PbI_3$ powder with KOH in N_2 glove box (Supplementary Figure 1). The black $CH_3NH_3PbI_3$ powder quickly changes to a white sticky product within three minutes of stirring. X-ray diffraction (XRD) results of the corresponding dried powder suggest the existence of PbO and KI (Supplementary Figure 1c). Based on these results, we propose a reaction of perovskites with KOH as follows:

$$CH_3NH_3PbI_3 + 3KOH \rightarrow Pb(OH)_2 + CH_3NH_2 + H_2O + 3KI \qquad (1)$$

Supplementary Note 2

Organic interface modifiers showed the ability to modify the work function when employed with ETLs or electrodes. For example, similar to EDTAK, EDTA-Na has also been used as interlayer to modify ITO substrate for organic solar cells.[28] Here, EDTAK can also serve several purposes other than just reacting with KOH, and therefore it can be considered as a general interface modifier for other ETLs as well. In our results, the fact that Sn 3*d* peaks in XPS (Figure 2b) does not shift significantly indicates a weak chemical interaction between EDTAK and SnO_2. This negligible shift in XPS Sn 3*d* core levels are also reflected in the electronic states corresponding to valence electrons of SnO_2 that can be probed by UPS. The VBM of pristine SnO_2 and EDTAK-SnO_2 samples are –3.64 eV and –3.74 eV, respectively (i.e., difference of only 0.1 eV observed). On the basis of XPS and UPS analysis above, the shift in WF observed in our studies seems to be supported by the interfacial dipole phenomena (Supplementary Figure 2).[29] This interfacial layer is further confirmed by the observed N 1*s* peak in XPS of the EDTAK treated SnO_2 films (Figure 2a). An alternative explanation is contact doping phenomena that leads to interfacial charge accumulation.[29,30] The charge accumulation not only affects WF but also affects VBM simultaneously. When comparing the pristine SnO_2 and EDTAK modified SnO_2, the changes in VBM were negligible. Therefore, doping effects can be excluded.

Supplementary Note 3

A high content of EA on the surface of perovskite layer can help achieve a balance between stability and device performance. Although the very high contents of EA show improved stability of perovskite bulk film, but it also leads to deterioration in device performance that limits its application.[31-33] To explore the optimized EA/MA composition for surface engineering, mixed EAI/MAI = x : (1−x) with different molar ratios were reacted with PbI_2 films via a two-step method. Supplementary Figure 7a shows the XRD spectra of the obtained $MA_{1-x}EA_xPbI_3$ films. It is found that when x = 0.1~0.4, the corresponding films show clear diffraction peaks at around 14° assigned to the perovskite phase. Note that no obvious signal lower than 10° is observed for all samples, indicating the trace amount of 2D perovskite within these films (Supplementary Figure 7a). The slight XRD peak shift from 14.03° in the case of x = 0 to 13.97° in the case of x = 0.4 indicates the partial substitution of MA^+ ions with larger EA^+ ions, which leads to slight expansion of the perovskite lattice (Supplementary Figure 7b). When x = 0.5, a small peak at about 11.77° is observed, which is assigned to the non-perovskite phase of $EAPbI_3$.[34] This non-perovskite peak at about 11.77° became much stronger for the x = 1.0 case, which corresponds to a yellow color non-perovskite film (Supplementary Figure 7c). The $MA_{0.5}EA_{0.5}PbI_3$ film-based devices showed much lower device performance than the cases of x = 0.1~0.4 (Supplementary Figure 7d). Considering the tradeoff between the EA content and device performance, the EA content of x = 0.4 is thus used for further studies. The EAI/MAI concentration for the $Cs_{0.05}FA_{0.54}MA_{0.41}Pb(I_{0.98}Br_{0.02})_3$ perovskite surface treatment was investigated as shown in Supplementary Figure 8 and Supplementary Table 4. It should be noted that a mixture of EAI and MAI was dissolved in a mixed solvent of isopropanol/N,N-dimethylformamide (volume ratio = 200:1). The mixed solvent is expected to partially dissolve the perovskite film top surface to enable a surface reconstruction and facilitate the interdiffusion of EAI/MAI modification on the top surface. Supplementary Figure 9 shows the XRD spectra of the $Cs_{0.05}FA_{0.54}MA_{0.41}Pb(I_{0.98}Br_{0.02})_3$ films with and without the EAI/MAI treatment, and no obvious signal lower than 10° is observed. The perovskite films with the EAI/MAI treatment showed slightly lower PbI_2 peak intensity and higher perovskite peak intensity than that of the pristine perovskite films. This observation suggests that additional ammonium halide in EAI/MAI treatment is likely to react with the slightly excessive PbI_2 and interact with the lead halide terminated surface to passivate defects, which might improve the device performance.[35]

Supplementary Note 4

To further quantitatively evaluate the reduction of the defect density via the EAI/MAI treatment, the space-charge-limited current (SCLC) measurements were conducted[36]. The defect density can be calculated according to the following equation:

$$N_{\mathrm{t}} = \frac{2\varepsilon\varepsilon_0 V_{\mathrm{TFL}}}{eL^2}$$

where ε and ε_0 are the dielectric constant of perovskite and the vacuum permittivity, respectively, V_{TFL} is the trap-filled limit voltage, L is the thickness of the perovskite films, and e is the elementary charge.

Supplementary Note 5

Au thin-films with a nominal thickness of 2 nm was deposited onto 4 different samples: (i) P3HT, (ii) spiro-OMeTAD, (iii) the P3HT : spiro-OMeTAD (0.5 mg : 4.5 mg in chlorobenzene), all of which were spin-coated on ITO/glass substrate. In addition, bare Au and bare P3HT films were also measured as the control samples. The corresponding binding energy of the Au $4f_{7/2}$ peak (Supplementary Figure 22a) was at ~84.1 eV for the Au/(P3HT+spiro-OMeTAD sample, and ~84.0 eV for the Au/P3HT sample and Au/spiro-OMeTAD sample. As comparison, the bare Au film (20 nm) showed the Au $4f_{7/2}$ peak at ~84.0 eV. To investigate the interaction between the S-headgroup in P3HT and Au, we analyzed the S 2*p* core levels (Supplementary Figure 22b) by fitting Gaussian-Lorentzian functions after background subtraction corresponding to the inelastic scattering processes. For the Au/(P3HT+spiro-OMeTAD) and Au/P3HT samples, the S 2*p* spectra were composed of S $2p_{3/2}$ and S $2p_{1/2}$ doublet peaks that appeared at ~163.9 eV and ~165.1 eV, respectively, with the intensity ratio of 2:1, as expected based on the spin-orbit splitting effect.[37-39] As the reference, the bare P3HT film showed the S $2p_{3/2}$ and S $2p_{1/2}$ peaks at ~164.0 eV and ~165.2 eV, respectively, which is in good agreement with literature values.[40-42] Castner et al. have shown that self-assembled monolayers of alkanethiols deposited on Au(111) surfaces showed two doublets. Typical S $2p_{3/2}$ binding energies corresponding to pristine alkanethiols appear between 163 eV and 164 eV. The self-assembly (i.e., the strong S-Au interaction) was confirmed by the decrease of the S $2p_{3/2}$ binding energies to 162 eV. Therefore, in our studies (Supplementary Figure 22), the doublet peaks correspond majorly to the S-C bonding in P3HT. Although small, the binding energy shifts to lower values in the case of the Au/(P3HT+spiro-OMeTAD) and Au/P3HT samples compared to the reference P3HT sample, which indicates a charge transfer process from the Au surface to the S-headgroup of P3HT. This charge transfer is also corroborated by the slight Au $4f_{7/2}$ peak binding energy shift towards higher values for the Au/(P3HT+spiro-OMeTAD) sample compared to the bare Au film. Kim et al.[43] reported that the HTL composed of mixed spiro-OMeTAD and P3HT exhibited a vertical phase separation. The hydrophobic P3HT was more distributed near the surface, while the hydrophilic spiro-OMeTAD was majorly distributed near the perovskite layer. The mixed P3HT:spiro-OMeTAD HTL has two advantages: (1) the contact of spiro-OMeTAD with the perovskite leads to enhanced PCEs[44] and (2) the hydrophobic P3HT interacting with the top Au layer helps enhance the stability against Au diffusion into the perovskite layer.

Supplementary Note 6

The quick burn-in degradation followed by a slight increase phenomenon in stability of encapsulated perovskite solar cells has been observed in several reports.[11,45] The stability of another two encapsulated ITO/SnO_2-EDATK/PVSK(EAMA)/spiro-P3HT/Au PSMs are shown in Supplementary Figure 28. All the three modules show a quick burn-in degradation. In contrast, the unencapsulated device does not show such quick burn-in degradation. Based on above observation, the quick burn-in is speculated to be assigned to the degradation in an encapsulated environment. In early reports, the burn-in phenomenon in long-term stability profiles of perovskite solar cells was assigned to TiO_2/PVSK-mediated degradation in the PVSK layer, leading to redistribution of Cs^+ and FA^+.[46,47] When TiO_2 was replaced by SnO_2, the stability could be enhanced with decreased initial burn-in process.[48] In our encapsulated and unencapsulated PSM, the difference is the parylene-glass encapsulation. Considering the complexity of stability profile, we speculated that the encapsulation related factors induced such observed stability evolution, and the probable causes are discussed as follows:

1) **Thermal effect**. Because in the case of encapsulated PSMs, the parylene and glass encapsulation might avoid the direct contact of the active films with N_2 flow, when compared with encapsulated PSMs, the unencapsulated PSM might have a slightly better heat exchange, which may suppress the initial degradation. In contrast, the encapsulated PSM have inferior heat exchange N_2 flow, which leads to faster initial burn-in decay.
2) **Perovskite decomposition.** It has been reported that I_2 can be generated via a photodecomposition reaction of perovskite during the working condition.[49] The generated I_2 can trigger further decomposition of perovskite.[50] For the unencapsulated PSM, because the initial generated I_2 can be partially blown away by the N_2 flow, the I_2 induced degradation is expected to be reduced during the initial degradation. In contrast, for the encapsulated PSM, the initially generated I_2 is kept in the closed system, which leads to faster perovskite decomposition at the initial stage, and thus a quicker burn-in for encapsulated PSMs. But once the released I_2 amount has reached a certain concentration, the thermodynamic equilibrium is established, and the I_2 related reaction slows down or even turns back to form perovskite via the reversible reaction, which is corresponding to the slow increase at a later stage of the stability tracking evolution.
3) **Property change of HTL as a function of atmosphere.** A previous study from our group reveals that the air exposure largely affects the conductivity and interface energy

level variations of the spiro-OMeTAD layer.[51] This is because the gas species i.e., O_2 and H_2O in ambient air have an influence on the distribution of the dopant, i.e., LiTFSI within the HTL.[51-55] For the unencapsulated PSMs, the O_2 and H_2O residues diffused within the HTL layer during ambient exposure have not been fully removed, and will keep affecting the redistribution of LiTFSI to dope HTL to enable good charge transport properties. For the encapsulated PSMs, the pumping process of the parylene encapsulation facilitates the removal of physically absorbed O_2 and H_2O. The residual amount of O_2 and H_2O within the HTL in encapsulated PSMs is much lower than that of the unencapsulated PSM. This will cause poor conductivity and/or interface energy level variations of the THL at the beginning, which leads to a slow recovery of the encapsulated PSM performance after the quick burn-in.

Supplementary Note 7

The possible reasons for improved stability with parylene encapsulation are because of the multiple effects of parylene encapsulation on PSM stability. First, parylene encapsulation was conducted under a relative low pressure. The physically adsorbed species, such as H_2O and O_2, in air are expected to be partially removed during the pumping process during the parylene encapsulation. This may benefit stability improvement. The second effect is related to generation of the volatile species as a result of perovskite material degradation, where parylene may prevent leakage of volatile products released from the perovskite. It has been revealed that perovskite undergoes several reversible and irreversible pathways under simulated sunlight irradiation.[49,56,57] This means that the reversible pathway will tend to proceed towards the degradation direction for unencapsulated PSMs. In the case of encapsulated PSMs, parylene encapsulation serves as an enclosure to keep all these volatile products within the PSM to form a thermodynamically closed system, which helps reverse pathways towards the formation of perovskite side.[57] In this way, a dynamic balance is formed and reversible degradation is minimized, which we believe is another key reason why parylene encapsulation can significantly improve device stability under dry nitrogen. Note that the perovskite material used in the current study is a perovskite material with Cs-FA-MA mixed cations and I-Br mixed halides (i.e., not pure $MAPbI_3$), but it is reasonable to expect that similar reversible reactions with volatile species as products are also present for such perovskite materials with mixed cations and mixed halides. On the other hand, parylene encapsulation also avoids the direct exposure of perovskite and HTL to air at the regions of scribed series interconnections, which may also partially contribute to the stability improvement.[25]

Supplementary References

1 Moon, S. *et al.* Laser-Scribing Patterning for the Production of Organometallic Halide Perovskite Solar Modules. *IEEE Journal of Photovoltaics* **5**, 1087-1092 (2015).

2 Palma, A. L. *et al.* Laser-Patterning Engineering for Perovskite Solar Modules With 95% Aperture Ratio. *IEEE Journal of Photovoltaics* **7**, 1674-1680 (2017).

3 Rakocevic, L. *et al.* Interconnection Optimization for Highly Efficient Perovskite Modules. *IEEE Journal of Photovoltaics* **7**, 404-408 (2017).

4 Domanski, K., Alharbi, E. A., Hagfeldt, A., Grätzel, M. & Tress, W. Systematic investigation of the impact of operation conditions on the degradation behaviour of perovskite solar cells. *Nature Energy* **3**, 61-67 (2018).

5 Seo, J. *et al.* Benefits of very thin PCBM and LiF layers for solution-processed p–i–n perovskite solar cells. *Energy & Environmental Science* **7**, 2642-2646 (2014).

6 Heo, J. H., Han, H. J., Kim, D., Ahn, T. K. & Im, S. H. Hysteresis-less inverted $CH_3NH_3PbI_3$ planar perovskite hybrid solar cells with 18.1% power conversion efficiency. *Energy & Environmental Science* **8**, 1602-1608 (2015).

7 Chiang, C.-H., Lin, J.-W. & Wu, C.-G. One-step fabrication of a mixed-halide perovskite film for a high-efficiency inverted solar cell and module. *Journal of Materials Chemistry A* **4**, 13525-13533 (2016).

8 Agresti, A. *et al.* Graphene Interface Engineering for Perovskite Solar Modules: 12.6% Power Conversion Efficiency over 50 cm^2 Active Area. *ACS Energy Letters* **2**, 279-287 (2017).

9 Bu, T. *et al.* A novel quadruple-cation absorber for universal hysteresis elimination for high efficiency and stable perovskite solar cells. *Energy & Environmental Science* **10**, 2509-2515 (2017).

10 Qiu, L. *et al.* Scalable Fabrication of Stable High Efficiency Perovskite Solar Cells and Modules Utilizing Room Temperature Sputtered SnO_2 Electron Transport Layer. *Advanced Functional Materials* **29**, 1806779 (2018).

11 Jung, E. H. *et al.* Efficient, stable and scalable perovskite solar cells using poly(3-hexylthiophene). *Nature* **567**, 511-515 (2019).

12 Deng, Y. *et al.* Surfactant-controlled ink drying enables high-speed deposition of perovskite films for efficient photovoltaic modules. *Nature Energy* **3**, 560-566 (2018).

13 Di Giacomo, F. *et al.* Up-scalable sheet-to-sheet production of high efficiency perovskite module and solar cells on 6-in. substrate using slot die coating. *Solar Energy*

Materials and Solar Cells **181**, 53-59 (2018).

14 Longhua, C. *et al.* Large area perovskite solar cell module. *Journal of Semiconductors* **38**, 014006 (2017).

15 Priyadarshi, A. *et al.* A large area (70 cm^2) monolithic perovskite solar module with a high efficiency and stability. *Energy & Environmental Science* **9**, 3687-3692 (2016).

16 Hu, Y. *et al.* Stable Large-Area (10 × 10 cm^2) Printable Mesoscopic Perovskite Module Exceeding 10% Efficiency. *Solar RRL* **1**, 1600019 (2017).

17 Grancini, G. *et al.* One-Year stable perovskite solar cells by 2D/3D interface engineering. *Nature Communications* **8**, 15684 (2017).

18 Heo, J. H., Lee, M. H., Jang, M. H. & Im, S. H. Highly efficient $CH_3NH_3PbI_{3-x}Cl_x$ mixed halide perovskite solar cells prepared by re-dissolution and crystal grain growth via spray coating. *Journal of Materials Chemistry A* **4**, 17636-17642 (2016).

19 Chen, H. *et al.* A solvent- and vacuum-free route to large-area perovskite films for efficient solar modules. *Nature* **550**, 92-95, doi:10.1038/nature23877 (2017).

20 Tian, S. *et al.* A facile green solvent engineering for up-scaling perovskite solar cell modules. *Solar Energy* **183**, 386-391 (2019).

21 Qiu, L. *et al.* Hybrid Chemical Vapor Deposition Enables Scalable and Stable Cs-FA Mixed Cation Perovskite Solar Modules with a Designated Area of 91.8 cm^2 Approaching 10% Efficiency. *Journal of Materials Chemistry A* **7**, 6920-6929 (2019).

22 Luo, L. *et al.* Large-area perovskite solar cells with $Cs_xFA_{1-x}PbI_{3-x}Br_x$ thin film deposited by vapor-solid reaction method. *Journal of Materials Chemistry A* **6**, 21143-21148 (2018).

23 Bu, T. *et al.* Sub-sized monovalent alkaline cations enhanced electrical stability for over 17% hysteresis-free planar perovskite solar mini-module. *Electrochimica Acta* **306**, 635-642 (2019).

24 Li, K. *et al.* Influence of Hot Spot Heating on Stability of Large Size Perovskite Solar Module with a Power Conversion Efficiency of ∼14%. *ACS Applied Energy Materials* **1**, 3565-3570 (2018).

25 Bi, E. *et al.* Efficient Perovskite Solar Cell Modules with High Stability Enabled by Iodide Diffusion Barriers. *Joule* **3**, 1-13 (2019).

26 Bu, T. *et al.* Universal passivation strategy to slot-die printed SnO_2 for hysteresis-free efficient flexible perovskite solar module. *Nature Communications* **9**, 4609 (2018).

27 Chen, Y. *et al.* Impacts of alkaline on the defects property and crystallization kinetics in perovskite solar cells. *Nature Communications* **10**, 1112 (2019).

28 Li, X., Zhang, W., Wang, X., Gao, F. & Fang, J. Disodium Edetate As a Promising Interfacial Material for Inverted Organic Solar Cells and the Device Performance Optimization. *ACS Applied Materials & Interfaces* **6**, 20569-20573 (2014).

29 Wu, Z. *et al.* Highly Efficient and Stable Perovskite Solar Cells via Modification of Energy Levels at the Perovskite/Carbon Electrode Interface. *Adv. Mater.* **31**, 1804284 (2019).

30 Wang, S., Sakurai, T., Wen, W. & Qi, Y. B. Energy Level Alignment at Interfaces in Metal Halide Perovskite Solar Cells. *Adv. Mater. Interfaces* **5**, 1800260 (2018).

31 Im, J.-H., Chung, J., Kim, S.-J. & Park, N.-G. Synthesis, structure, and photovoltaic property of a nanocrystalline 2H perovskite-type novel sensitizer ($CH_3CH_2NH_3$)PbI_3. *Nanoscale Research Letters* **7**, 353 (2012).

32 Peng, W. *et al.* Engineering of $CH_3NH_3PbI_3$ Perovskite Crystals by Alloying Large Organic Cations for Enhanced Thermal Stability and Transport Properties. *Angewandte Chemie International Edition* **55**, 10686-10690 (2016).

33 Zhou, J. *et al.* Efficient ambient-air-stable HTM-free carbon-based perovskite solar cells with hybrid 2D–3D lead halide photoabsorbers. *Journal of Materials Chemistry A* **6**, 22626-22635 (2018).

34 Zhang, Y., Kim, S.-G., Lee, D., Shin, H. & Park, N.-G. Bifacial stamping for high efficiency perovskite solar cells. *Energy & Environmental Science* **12**, 308-321 (2019).

35 Luo, D. *et al.* Enhanced photovoltage for inverted planar heterojunction perovskite solar cells. *Science* **360**, 1442-1446 (2018).

36 Son, D.-Y. *et al.* Universal Approach toward Hysteresis-Free Perovskite Solar Cell via Defect Engineering. *Journal of the American Chemical Society* **140**, 1358-1364 (2018).

37 Noh, J. *et al.* High-Resolution STM and XPS Studies of Thiophene Self-Assembled Monolayers on Au(111). *The Journal of Physical Chemistry B* **106**, 7139-7141 (2002).

38 Liu, G., Rodriguez, J. A., Dvorak, J., Hrbek, J. & Jirsak, T. Chemistry of sulfur-containing molecules on Au(111): thiophene, sulfur dioxide, and methanethiol adsorption. *Surface Science* **505**, 295-307 (2002).

39 Rodriguez, J. A. *et al.* Desulfurization of Thiophene on Au/TiC(001): Au−C Interactions and Charge Polarization. *Journal of the American Chemical Society* **131**, 8595-8602 (2009).

40 Castner, D. G., Hinds, K. & Grainger, D. W. X-ray Photoelectron Spectroscopy Sulfur 2p Study of Organic Thiol and Disulfide Binding Interactions with Gold Surfaces. *Langmuir* **12**, 5083-5086 (1996).

41 Shamieh, B., Obuchovsky, S. & Frey, G. L. Spontaneous generation of interlayers in OPVs with silver cathodes: enhancing Voc and lifetime. *Journal of Materials Chemistry C* **4**, 1821-1828 (2016).

42 Wei, H., Scudiero, L. & Eilers, H. Infrared and photoelectron spectroscopy study of vapor phase deposited poly (3-hexylthiophene). *Applied Surface Science* **255**, 8593-8597 (2009).

43 Kim, G.-W., Kang, G., Malekshahi Byranvand, M., Lee, G.-Y. & Park, T. Gradated Mixed Hole Transport Layer in a Perovskite Solar Cell: Improving Moisture Stability and Efficiency. *ACS Applied Materials & Interfaces* **9**, 27720-27726 (2017).

44 Hawash, Z., Ono, L. K. & Qi, Y. B. Recent Advances in Spiro‐MeOTAD Hole Transport Material and Its Applications in Organic–Inorganic Halide Perovskite Solar Cells. *Advanced Materials Interfaces* **5**, 1700623 (2018).

45 Zheng, X. *et al.* Managing grains and interfaces via ligand anchoring enables 22.3%-efficiency inverted perovskite solar cells. *Nature Energy* **5**, 131–140 (2020).

46 Tress, W. *et al.* Performance of perovskite solar cells under simulated temperature-illumination real-world operating conditions. *Nature Energy* **4**, 568-574 (2019).

47 Domanski, K. *et al.* Migration of cations induces reversible performance losses over day/night cycling in perovskite solar cells. *Energy & Environmental Science* **10**, 604–613 (2017).

48 Christians, J. A. *et al.* Tailored interfaces of unencapsulated perovskite solar cells for >1,000 hour operational stability. *Nature Energy* **3**, 68-74 (2018).

49 Juarez-Perez, E. J. *et al.* Photodecomposition and thermal decomposition in methylammonium halide lead perovskites and inferred design principles to increase photovoltaic device stability. *Journal of Materials Chemistry A* **6**, 9604-9612 (2018).

50 Wang, S., Jiang, Y., Juarez-Perez, Emilio J., Ono, Luis K. & Qi, Y B.. Accelerated degradation of methylammonium lead iodide perovskites induced by exposure to iodine vapour. *Nature Energy* **2**, 16195 (2016).

51 Hawash, Z., Ono, L. K. & Qi, Y. B. Moisture and Oxygen Enhance Conductivity of LiTFSI-Doped Spiro-MeOTAD Hole Transport Layer in Perovskite Solar Cells. *Advanced Materials Interfaces* **3**, 1600117 (2016).

52 Hawash, Z., Ono, L. K., Raga, S. R., Lee, M. V. & Qi, Y. B. Air-Exposure Induced Dopant Redistribution and Energy Level Shifts in Spin-Coated Spiro-MeOTAD Films. *Chemistry of Materials* **27**, 562-569 (2015).

53 Juarez-Perez, E. J. *et al.* Role of the Dopants on the Morphological and Transport Properties of Spiro-MeOTAD Hole Transport Layer. *Chemistry of Materials* **28**, 5702-5709 (2016).

54 Ono, L. K. *et al.* Air-Exposure-Induced Gas-Molecule Incorporation into Spiro-MeOTAD Films. *The Journal of Physical Chemistry Letters* **5**, 1374-1379 (2014).

55 Ono, L. K. *et al.* Pinhole-free hole transport layers significantly improve the stability of MAPbI3-based perovskite solar cells under operating conditions. *Journal of Materials Chemistry A* **3**, 15451-15456 (2015).

56 Juarez-Perez, E. J., Ono, L. K. & Qi, Y. B. Thermal degradation of formamidinium based lead halide perovskites into sym-triazine and hydrogen cyanide observed by coupled thermogravimetry-mass spectrometry analysis. *Journal of Materials Chemistry A* **7**, 16912-16919 (2019).

57 Brinkmann, K. O. *et al.* Suppressed decomposition of organometal halide perovskites by impermeable electron-extraction layers in inverted solar cells. *Nature Communications* **8**, 13938 (2017).